remote sensing

MDPI

Article

A NIST-Traceable Lab-to-Sky Spectral and Radiometric Calibration for NASA's High-Altitude Airborne Hyperspectral Pushbroom Imager for Cloud and Aerosol Research and Development (PICARD)

Gary D. Hoffmann [1,2,*], Thomas Ellis [1,2], Haiping Su [1,2], Alok Shrestha [1,2], Julia A. Barsi [3], Roseanne Dominguez [1,2], Eric Fraim [1,2], James Jacobson [1,2], Steven Platnick [4,5], G. Thomas Arnold [6,7], Kerry Meyer [7] and Jessica L. McCarty [8]

1 Airborne Sensor Facility, Earth Science Division, NASA Ames Research Center, Moffett Field, CA 94035, USA; thomas.ellis@nasa.gov (T.E.); su@baeri.org (H.S.); alok.k.shrestha@nasa.gov (A.S.); roseanne.dominguez@nasa.gov (R.D.); eric.w.fraim@nasa.gov (E.F.); james.d.jacobson@nasa.gov (J.J.)
2 Bay Area Environmental Research Institute, P.O. Box 25, Moffett Field, CA 94035, USA
3 Biospheric Sciences Laboratory, NASA Goddard Space Flight Center, Greenbelt, MD 20771, USA; julia.a.barsi@nasa.gov
4 Earth Science Division, NASA Goddard Space Flight Center, Greenbelt, MD 20771, USA; steven.e.platnick@nasa.gov
5 EOS Project Science Office, NASA Goddard Space Flight Center, Greenbelt, MD 20771, USA
6 Science Systems and Applications Inc., 10210 Greenbelt Rd, Lanham, MD 20706, USA; tom.arnold@nasa.gov
7 Climate and Radiation Laboratory, NASA Goddard Space Flight Center, Greenbelt, MD 20771, USA; kerry.meyer@nasa.gov
8 Earth Science Division, NASA Ames Research Center, Moffett Field, CA 94035, USA; jessica.l.mccarty-kern@nasa.gov
* Correspondence: gary.d.hoffmann@nasa.gov

Highlights

What are the main findings?

- Spectral and radiometric lab calibrations for a new airborne hyperspectral imager agree well in comparison to multiple real-world reference data sources and targets.
- Spectral stray light characterization facilitates radiometric calibration independent of large spectral differences between incandescent lab sources and solar illumination.

What are the implications of the main findings?

- Characterizing spectral stray light using a GLAMR-like setup with tunable lasers is highly beneficial for diffraction grating spectrometers used for remote sensing.
- PICARD lab calibrations are validated at high altitudes for environmental remote sensing and testing cloud and aerosol retrieval algorithms or new sensor designs.

Check for updates

Academic Editors: Stefano Pignatti and Yaqiang Wang

Received: 6 March 2026
Revised: 1 April 2026
Accepted: 8 April 2026
Published: 14 April 2026

Copyright: © 2026 by the authors. Licensee MDPI, Basel, Switzerland. This article is an open access article distributed under the terms and conditions of the Creative Commons Attribution (CC BY) license.

Abstract

The Pushbroom Imager for Cloud and Aerosol Research and Development (PICARD) visible through shortwave infrared imaging spectrometer was developed to carry a calibration laboratory environment to high altitudes, while also providing high-dynamic-range bright cloud-top radiance measurements across a field of view just under 50 degrees. The in-flight performance of this new spectroradiometer was validated in comparison to multiple reference data sources and targets using imagery collected aboard NASA's ER-2 high-altitude aircraft during the Western Diversity Time Series (WDTS) airborne science campaign in April 2023 and the September 2024 Plankton, Aerosol, Cloud, and ocean Ecosystem (PACE) Postlaunch Airborne eXperiment (PACE-PAX), both operating out of southern California.

PICARD measurements from flights over Railroad Valley Playa, Nevada, USA, were compared to high-resolution radiance spectra of the dry lakebed provided by the Radiometric Calibration Network (RadCalNet) Working Group. Direct comparison to satellite cloud radiometry was enabled by the ER-2 flying in coordination with simultaneous overpasses of the Terra, Aqua, and NOAA-20 Earth-observing satellites during WDTS and with the PACE observatory during PACE-PAX. To account for large spectral differences between incandescent laboratory sources and solar illumination, PICARD calibration relies on measurements using the Goddard Laser for Absolute Measurements of Radiance (GLAMR) to characterize and minimize spectral stray light from the instrument's twin Offner grating spectrometers. Good agreement in comparison to reference measurements demonstrates PICARD's ability to provide imagery for environmental science or for testing new sensor designs and retrieval algorithms for cloud and aerosol research with verified laboratory calibrations at high altitudes.

Keywords: imaging spectroscopy; hyperspectral imagery; stray light; remote sensing; visible and near infrared (VNIR) spectroscopy; shortwave infrared (SWIR) spectroscopy; PICARD; GLAMR; NASA; PACE-PAX; calibration; validation; intersensor comparison

1. Introduction

The Airborne Sensor Facility (ASF) at NASA Ames Research Center (ARC) in Moffett Field, California, is responsible for the development, calibration, and operation of several facility instruments designed to fly aboard NASA science aircraft. These include the 50-channel visible through thermal infrared imager called the MODIS/ASTER Airborne Simulator (MASTER) [1,2] and the similar 38-channel enhanced MODIS Airborne Simulator (eMAS) [3,4], both of which were originally designed as airborne analogs for the spaceborne Moderate Resolution Imaging Spectroradiometer (MODIS), a key sensor of NASA's Earth Observing System (EOS). In 2010, ASF proposed a relatively inexpensive and compact design for a visible through near and shortwave infrared (VNIR/SWIR) hyperspectral imager to fly in companion with eMAS. This hyperspectral imager ultimately became the Pushbroom Imager for Cloud and Aerosol Research and Development (PICARD) [5].

PICARD was developed to support scientific studies of clouds and aerosols, providing 206 channels of imagery from 375 nm to 2400 nm to supplement the 25 eMAS channels in the same spectral region and 13 eMAS channels that spectrally approximate the longer infrared and thermal imaging capabilities of MODIS. Following a series of eight engineering test flights in 2017 through 2022 and 12 validation flights during the Western Diversity Time Series (WDTS) campaign in 2023, PICARD was selected to participate in the PACE Postlaunch Airborne eXperiment (PACE-PAX) in September 2024 [6]. PACE-PAX was a suborbital validation campaign for the Phytoplankton, Aerosol, Cloud, and ocean Ecosystem (PACE) satellite that was launched in February 2024 [7]. The WDTS and PACE-PAX campaigns were both based out of NASA Armstrong Flight Research Center (AFRC) in southern California, employing the high-altitude ER-2 research aircraft to fly over a diverse selection of targets around the American Southwest and Northeastern Pacific Ocean (Figure 1).

The PACE satellite hosts the Ocean Color Instrument (OCI) [8] that provides continuous hyperspectral imagery across 282 channels from the ultraviolet at 315 nm to the near-infrared at 895 nm, as well as 9 additional discrete SWIR channels from 940 nm to 2260 nm. Airborne imagery can be used to create pseudo-satellite imagery while hosting additional instruments capable of measuring the physical properties that are ultimately

the goal of the satellite imagery. PICARD imagery served as the basis for pseudo-satellite imagery for OCI's discrete SWIR channels (940–2260 nm) as well as the high-radiance end of the OCI dynamic range in the VNIR (315–895 nm) for PACE-PAX, whereas imagery from the 350–1050 nm Portable Remote Imaging Spectrometer (PRISM) [9] operated by the NASA Jet Propulsion Laboratory (JPL) provided the basis for pseudo-satellite imagery for OCI's contiguous hyperspectral VNIR channels over the majority of the OCI dynamic range. The ER-2 also hosted airborne analog instruments for other PACE sensors, as well as a cloud and aerosol profiling lidar system. Other instruments aboard the CIRPAS Twin Otter aircraft collected low-altitude in situ measurements of the atmosphere. Both aircraft were flown in coordination with surface vessels and AERONET sites collecting a variety of measurements [10], offering an exceptional opportunity to validate remote sensing retrievals using hyperspectral imagery of the Earth's surface in comparison to air and water samples collected in situ or from the surface. All data collected from this campaign, including PICARD imagery, is available via open access (see Section 4.3).

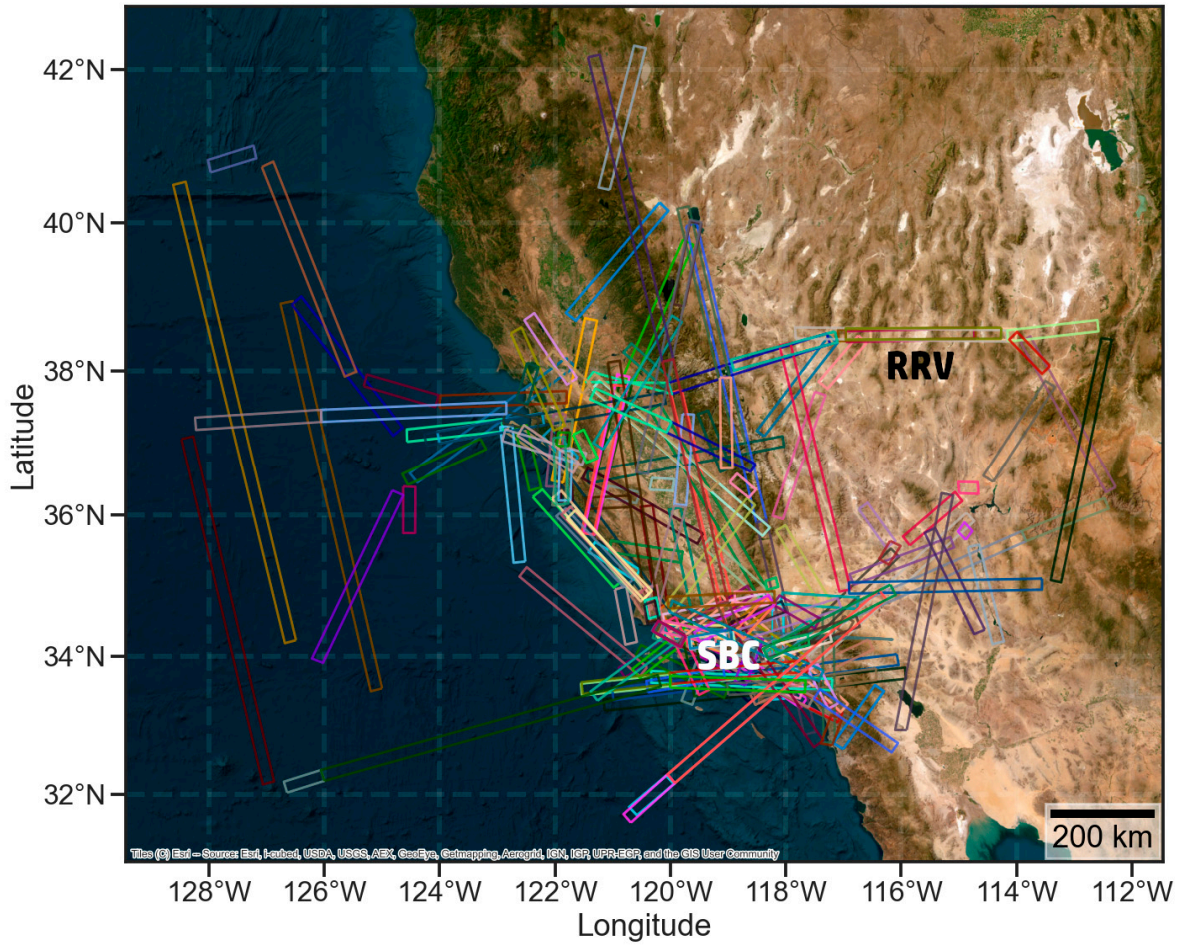

Figure 1. Pushbroom Imager for Cloud and Aerosol Research and Development (PICARD) flight tracks during the September 2024 Plankton, Aerosol, Cloud, ocean Ecosystem (PACE) Postlaunch Airborne eXperiment (PACE-PAX) satellite validation airborne science campaign. The locations of Railroad Valley (RRV) and Santa Barbara Channel (SBC) are shown. Surface measurements were collected by a variety of scientific assets in SBC. The long NNW-SSE tracks generally correspond to satellite overpasses, especially over open ocean. Flights were opportunistically planned to overpass stationary AERONET sites on land located at several locations scattered around the region.

This manuscript presents the PICARD airborne hyperspectral imager, the NIST-traceable spectral and radiometric calibration used for PICARD radiance measurements,

and the subsequent data delivered to the PACE-PAX data repository in March 2025. The National Institute for Standards and Technology (NIST) is a non-regulatory agency of the U.S. Department of Commerce that establishes traceability to the International System of Units (SI) so that measurement results can be related to an SI reference through an unbroken chain of calibrations [11]. Only two NASA centers currently host NIST-traceable calibration labs for Earth's reflective spectral range that are available for use by outside instruments, with four labs at the Goddard Space Flight Center (GSFC) and ASF at ARC recently participating in annual intercalibration round robins for cross-validating each lab's sources, detectors, and methods [12].

Early attempts to characterize the spectroradiometric performance of PICARD used a monochromator with an incandescent lamp source historically used for the multispectral instruments eMAS and MASTER but were frustrated by stronger stray light sensitivities inherent to the hyperspectral grating spectrometers. PICARD radiometric calibration therefore relies on measurements using the Goddard Laser for Absolute Measurements of Radiance (GLAMR) [13] at GSFC to account for spectral stray light and derive calibration gains that are independent of large spectral differences between our incandescent laboratory source and solar illumination. Section 2 presents the PICARD instrument design, the GLAMR lab, the PICARD/GLAMR experiment in February 2024, the laboratory radiometric calibration that converts instrument response to SI radiance units, and the spectral stray light correction algorithm we used for PICARD following the method first described by [14]. In Section 3, we present in-flight radiance data compared to the Radiometric Calibration Network (RadCalNet) automated calibration/validation site at the Railroad Valley (RRV) dry lakebed in Nevada [15] and compared to satellite imagery over marine stratus clouds. The benefit of accurately characterizing and compensating for spectral stray light in remote sensing grating spectrometers using a GLAMR-like setup is illustrated by these comparisons before and after implementing the stray light correction in our calibration method. In Section 4, we discuss the stray light correction method and contextualize the real-world validation results. We also include some technical notes for users of PICARD data files. Section 5 concludes with the implications for future PICARD science and missions. This manuscript provides a detailed description of the PICARD instrument, our GLAMR-based spectral stray light correction method, and our assessment of PICARD's ability to provide calibrated radiance measurements at high altitudes without relying on atmospheric radiative transfer modeling for vicarious calibration.

2. Materials and Methods

2.1. PICARD Instrument Design and Specifications

The PICARD instrument was developed by NASA ARC in partnership with Brandywine Photonics, LLC. of West Chester, PA, USA. The sensor uses two Offner spectrometers, features an all-reflective telescope with a 49.5° full field of view (FOV), a dichroic fold mirror, and a pressurized enclosure design emphasizing environmental control and radiometric stability monitoring at high altitudes [16]. A summary of the PICARD specifications is given in Table 1.

The instrument system supports a variety of data collection speeds and integration times, allowing it to acquire contiguous imagery at a variety of altitudes and ground speeds (Table 1). The system consists of the pressurized optical enclosure unit, a digital recording box (DRB), and a position and orientation sensor (POS) with masses of approximately 34 kg, 2 kg, and 7 kg, respectively. The PICARD optical enclosure occupies an approximate volume of 68 L. The DRB and POS units utilize approximately 30 cm of vertical space on a single shelf of a standard 48 cm mounting rack.

Table 1. Summary of key PICARD specifications.

Type:	VNIR-SWIR Airborne Imaging Spectrometer
Platform:	NASA ER-2, G-V, G-III, B200
Ground Speed:	Variable (depending on altitude)
Altitude:	1–20 km
Pixel Spatial Resolution:	5–50 m (depending on altitude)
Pixels per Spectral Band:	412 (binned and roll corrected)
Integration Time:	5.2–80 mSec (limited by frame rate/altitude)
Swath Width:	2–16 km (depending on altitude)
Field of View:	49.5°
Effective Focal Length	30.4 mm
Instantaneous FOV (cross track):	2.12 mrad (binned)
Instantaneous FOV (along track):	2.12 mrad
Roll Correction:	+/− 15°
Spectral Bands:	206 (digitized to 14-bit resolution)
VNIR Spectrometer:	64 15 nm FWHM bands, 375–990 nm
SWIR Spectrometer:	142 15 nm FWHM bands, 1.00–2.40 µm
Frame Rate:	6.25–100 Hz (depending on integration time)
Dimensions:	42 cm × 25 cm × 65 cm
Weight:	41 kg (34 kg PICARD + 2 kg DRB + 7 kg POS-AV)

The PICARD optical design consists of two separate hyperspectral spectrographs sharing a common telescope and slit to promote spatial co-registration (Figure 2). The telescope generates a single image at the spectrometer slit, at location "E" in Figure 2. After incoming light passes through the slit, the beam is split by a dichroic mirror, "F", that passes the longer wavelength light to the shortwave infrared (SWIR) spectrometer, "H", and reflects the shorter wavelength light into the visible-and-near-infrared (VNIR) spectrometer, "L". To achieve the relatively broad spectral range of the sensor with a 49.5° field of view matched to the Offner relay, an all-reflective telescope was designed to be image-space telecentric using a four-mirror anastigmat design, with minimized aspheric departure.

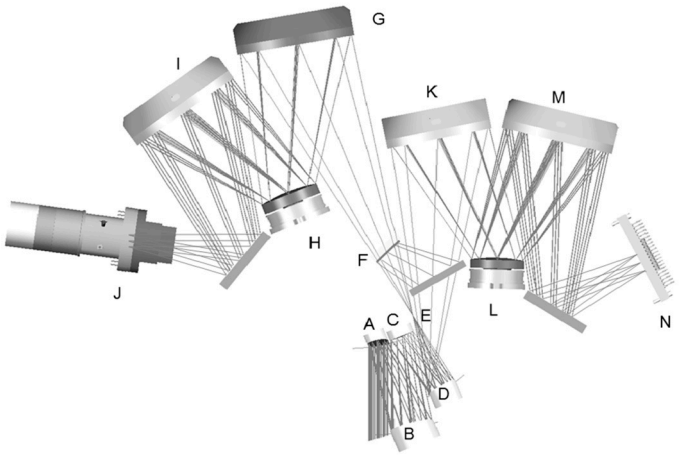

Figure 2. Schematic of PICARD sensor optics with representative ray trace. A–D: Telescope mirrors M1 to M4. E: Common slit. F: Dichroic mirror. G: SWIR asphere M1. H: SWIR grating. I: SWIR spherical M2. J: SWIR dewar. K, M: VNIR spherical mirrors M1 and M2. L: VNIR grating. N: VNIR detector. Optical flats not labeled.

The VNIR spectrometer is a traditional Offner design [17,18]. This consists of two concave, spherical mirrors (K and M in Figure 2) and a convex, spherical diffraction grating (L, Figure 2) focusing the spectrally dispersed image of the slit onto a 2-D array with 1-to-1 magnification. The detector is a Sarnoff CCD160-250-SFT, consisting of a 2048 × 256 silicon CCD array with a 16 µm pitch. To closely match the SWIR spectrometer spatial and

spectral dimension, the detector output is binned during processing in a 4 × 4 pattern to a 512 × 64 array, of which 412 binned across-track pixels are illuminated by the slit. The Sarnoff array is capable of operating at 1000 frames per second (fps). The maximum frame rate anticipated for deployment is 100 fps. For WDTS and PACE-PAX, the frame rate was set at 6.25 fps.

The CCD is a back-illuminated split frame transfer design with a 100% fill factor. It has a full well of 180,000 electrons with an expected read-out noise of less than 70 electrons and 32 analog taps. To reduce dark current and enhance radiometric stability, the temperature of the detector is controlled by a thermoelectric cooler (TEC).

The SWIR spectrometer is an Offner system modified to introduce a slight demagnification of 32:30 at the focal plane. The demagnification requirement is driven by the need to closely co-register the instantaneous FOV of pixels between the SWIR and VNIR spectrometers. The SWIR FPA has a 30 µm pitch; the VNIR FPA has 16 µm pixels that bin to match the slit dimension of 32 µm along track. The demagnification is achieved by pushing the SWIR M1 mirror (G, Figure 2) further from the SWIR M2 grating (H, Figure 2) than the SWIR M3 mirror (I, Figure 2). This departure from the stop symmetry of a 1:1 magnification Offner image relay introduces odd order aberrations that were corrected by adding a slight conic asphere to the M1 surface.

The SWIR detector is a Saturn HgCdTe focal-plane array consisting of 1000 × 256 pixels manufactured by Lynred (formerly Sofradir) of Palaiseau, France [19]. The detector resides in an Integrated Cooler Dewar Assembly (ICDA) maintained at a temperature of approximately 100 K. The detector output is binned during processing in a 2 × 1 pattern, with the spatial and spectral dimensions matching those of the VNIR spectrometer. Of the 500 binned across-track pixels, 412 are illuminated over 142 of the 256 pixels in the spectral dimension. The Saturn model uses a custom focal-plane electronics package to control the detector and convert the data into a format similar to Cameralink, resulting in a maximum frame rate of 150 fps. The detector has two gain modes, a low-gain mode with a full well of 1.6×10^6 electrons and 400 electrons read-out noise and a high-gain mode with a full well of 0.4×10^6 electrons and 150 electrons read-out noise. The Lynred detector allows for different gain settings to be applied to different spectral bands, which is used to optimize the signal-to-noise ratio across the SWIR spectrum.

2.2. The GLAMR System

The Goddard Laser for Absolute Measurements of Radiance (GLAMR) is a spectral and radiometric calibration and characterization facility [13], born out of technology developed for the NIST Spectral Irradiance and Radiance Calibration using Uniform Sources (SIRCUS) [20]. GLAMR uses a series of tunable lasers to provide both spectrally and radiometrically uniform, monochromatic illumination to an integrating sphere fitted with NIST-traceable monitoring radiometers [21,22]. A collection of laser systems allows GLAMR to generate any wavelength between 310 and 2500 nm with a broad dynamic range in power. The large integrating sphere provides flight-like viewing conditions (full field of view, full aperture). GLAMR provides calibration of an instrument's Absolute Spectral Response (ASR) [DN per W cm^{-2} sr^{-1}], which allows for the derivation of instrument responsivity, spectral response, linearity, and spectral stray light, among other characterizations.

The primary components of GLAMR are the broadly tunable fiber-coupled light sources, a large integrating sphere, monitoring radiometers and wavemeters, and a set of NIST-traceable transfer radiometers periodically recalibrated at NIST [23]. The whole system is controlled and monitored by an extensive software backend.

Tunable monochromatic light is generated by several optical parametric oscillators (OPO) and associated harmonic generators. The light from the laser systems is fiber-coupled

to a 76 cm polytetrafluoroethylene (PTFE)-coated integrating sphere with a 25 cm aperture. Three monitoring radiometers, referred to as Sphere Monitors, are permanently mounted to the integrating sphere, to provide a measurement of the radiance in the sphere as well as feedback to the laser system to stabilize the light source. The wavelength is measured on the laser table with one of several wavemeters to cover the entire spectral range. The integrating sphere is aligned with the instrument to be tested and the monochromatic light from the sphere flood-illuminates the instrument focal plane.

The GLAMR control system automates illumination cycles and wavelength tuning for efficient test operation. Direct communication between the GLAMR control system and the instrument control system allows for triggering instrument actions based on GLAMR laser activity. The time-stamped radiometer signal (converted to radiance) and the corresponding wavelength data are the primary deliverables of a GLAMR measurement campaign.

GLAMR offers several significant advantages over traditional spectral measurement systems for instrument-level testing. The signal is unpolarized, non-dispersive, with no spectral smile and is radiometrically uniform. The constant monitoring of radiance in the sphere provides for knowledge of changes in the calibration system versus changes across the instrument. And importantly, the flood illumination allows for the diagnosis of spectrally dependent instrument effects across the focal plane. This flood of photons compared to the relative trickle from the MFC beams allowed us to resolve the small out-of-band responsivity for each PICARD band across its entire spectral range.

2.3. The PICARD/GLAMR Experiment

ASF arranged to bring PICARD to the GLAMR lab at NASA Goddard in February 2024 with the primary goal of identifying and characterizing an inferred source of stray light that had eluded our own series of experiments with a multi-field collimator (MFC) setup at ASF (see Appendix A). Approximately 2000 samples were collected during the experiment, with GLAMR wavelengths spaced about 1 nm apart for PICARD's VNIR detector and across the dichroic (368 nm to 1050 nm) and about 2 nm apart for PICARD's SWIR detector (1050 nm to 2450 nm), with some additional samples collected to test linearity and gain settings, or to redo earlier sample attempts. Generally, 20 s of PICARD imagery was collected for each sample at 6.25 frames per second, so up to 125 frames were averaged together to calculate a mean response frame for each GLAMR sample wavelength. This response was then averaged in the across-track direction and divided by the measured GLAMR radiance to provide across-track mean PICARD responsivities for each spectral bin in DN per W cm^{-2} sr^{-1} at each wavelength.

This responsivity as a function of wavelength provides an estimate of the absolute PICARD spectral response functions (SRFs) for each band. The absolute response functions can be closely approximated by Gaussian functions for the dominant mode, which we estimated with least-squares Gaussian fits. We found exceptional agreement in the determination of band centers between our MFC results and the GLAMR dominant Gaussian modes. Our estimates of the FWHM for each band are significantly (~30%) higher based on the line spread functions and flood illumination provided by GLAMR compared to using the point illumination provided by the MFC experiment. However, the Gaussian approximation of the PICARD SRFs falls apart below 1% of the peak responsivity of each band, where broadband residual stray light begins to dominate. The stray light signature was most severe at ultraviolet (UV) wavelengths, where PICARD in-band absolute responsivity is low, and in scenes with high out-of-band spectral content. The problem is exacerbated by calibration sources that have low radiance in the UV range, where the detector quantum efficiency is more sensitive to the more abundant out-of-band, longer-wavelength photons.

But with well-characterized stray light distribution functions we can use information from every spectral band of PICARD to correct each spectral band of the instrument itself.

Highly accurate estimates of the band centers and widths are necessary to provide accurate measurements of radiance in reference to an incandescent laboratory source. PICARD's radiometric calibration relies on the spectral calibration output to enable comparison of the instrument's response over the ASF lab's 91 cm diameter broadband integrating sphere. This instrument response was compared against independent spectral radiance measurements of the sphere output using an OL750 spectroradiometer that was calibrated in reference to a NIST-traceable FEL standard lamp [24].

2.4. PICARD Level 1B Radiance

The raw PICARD instrument response intensities recorded to disk as digital numbers, or "Level 0" data, are mapped to radiance at aperture in units of W m^{-2} μm^{-1} sr^{-1} and tagged with geolocation metadata during the processing to Level 1B, following the naming convention for NASA's Earth Observing System Data and Information System (EOSDIS) data products [25]. Above 10,000 digital numbers (DN) on the VNIR detector, we observe analog saturation effects that cause instrument response to become nonlinear with input radiance. Below 10,000 DN, we use a linear model comprising a series of gain factors, g, to relate observed radiance, L, as a function of detector array row and column positions, r and c, to the digital response with illumination, d, and without illumination, d_0. That is,

$$L(r, c) = g(r, c) \cdot [d(r, c) - d_0(r, c)] \quad (1)$$

The individual pixel gains, g, can be further decomposed into across-track mean radiometric calibration factors, G, one per spectral row, and a non-uniformity correction (NUC) image, N, that serves to flatten across-track variations in detector responsivity. We then express the radiometric calibration factors relative to a corrected measured response vector, y_{meas}, as follows:

$$L(r, c) = G(r) \cdot N(r, c) \cdot [d(r, c) - d_0(r, c)] \quad (2)$$

$$y_{meas}(r, c) = N(r, c) \cdot [d(r, c) - d_0(r, c)] \quad (3)$$

$$L(r, c) = G(r) \cdot y_{meas}(r, c) \quad (4)$$

The first step is to estimate d_0, the instrument response to complete darkness. The PICARD instrument includes a shutter mirror for switching focus to a dark cavity used for radiometric stability monitoring (RSM). Each record cycle during flight and in the lab begins with a 20 s RSM sequence recording dark image frames before collecting scene imagery. Laboratory measurements of the integrating sphere with zero-lamp (0-lamp) illumination are also used as a dark reference. When the VNIR focal-plane array (FPA) is held at a constant temperature during instrument operation, the zero-point response has not been observed to vary. We used the 0-lamp average image frame to subtract the dark response for the VNIR detector. The dark response for the SWIR detector, however, was observed to vary with the temperature of the SWIR optical bench (Figure 3) and requires special processing, despite the SWIR FPA quickly reaching a constant temperature of 106.56 K +/− 0.01 K during operation. That is, the SWIR detector is held at a constant cryogenic temperature, but the SWIR dark response nonetheless varies in a way that is closely correlated with the readings of a thermal sensor attached to a nearby structural aluminum component, and we derived an empirical relationship to define SWIR d_0 based on these readings after we were unable to isolate the cause of this drift.

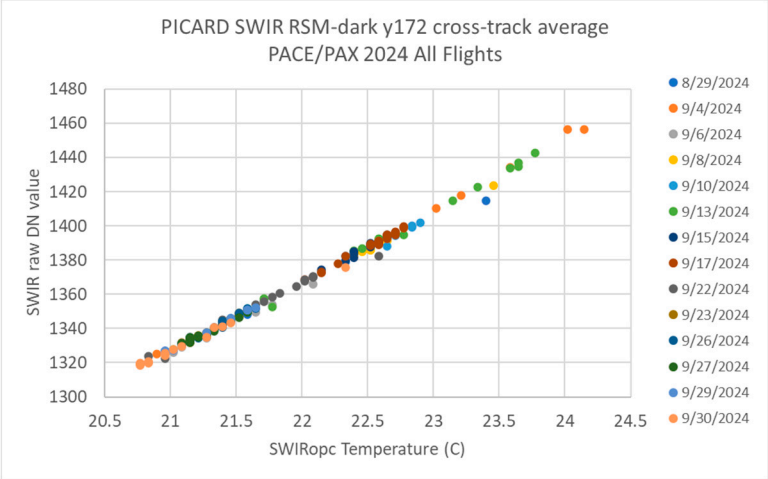

Figure 3. Dark response of the PICARD SWIR FPA during in-flight RSM shutter events. The across-track average for SWIR spectral row 172 (PICARD band 162, corresponding to light at the 1.88 μm wavelength) in the high-gain region of the detector is shown relative to the temperature of the SWIR optical bench sensor (SWIROpc). Each dot represents one record cycle, color-coded by NASA ER-2 flight date from the PACE-PAX campaign. The SWIR integration time was 40 ms for all flights.

Several thermal sensors are placed throughout the PICARD instrument for monitoring the health of various engineering subsystems, and the internal temperature of the instrument enclosure is controlled to a set point of 22.5 C and typically stays within 2 C of the set point during flight at a 20 km altitude. One of these sensors is attached to the SWIR optical bench, referred to as SWIROpc. The zero-illumination response of each SWIR detector element varies nearly linearly with the SWIROpc temperature in its normal operational range, which is typically close to the instrument set point (Figure 3). We use a linear model of SWIR dark response relative to SWIROpc temperature to estimate the amount to subtract from each image frame. For row and column positions, r and c, on the SWIR FPA, we define the dark response, d_0, to be the SWIROpc temperature, T, multiplied by thermal gains, h, and offset by the modeled dark response at zero Celsius, d_z:

$$d_0(r, c) = T \cdot h(r, c) + d_z(r, c) \quad (5)$$

The R^2 values of the linear fits for the SWIR dark response relative to temperature readings were above 0.98 across the detector using a series of 0-lamp images covering a temperature range of 20 to 24 C. The empirical thermal gains range from 9 to 12 DN per degree C in the low-gain region of the SWIR detector and are four times higher in the high-gain region. Values for d_z range from 400 to 700 DN, with the high-gain region offset by about 100 DN below the low-gain region. The resulting dark drift of 800 to 1400 DN represents ~5–10% of the SWIR dynamic range. The SWIROpc temperature readings have a precision of ~0.07 C, corresponding to a dark drift increment of less than 1 DN in the low-gain region of the FPA and 3–4 DN in the high-gain region. This amount is comparable to or below the instrument noise of ~2.4 DN in the low-gain and ~4.0 DN in the high-gain regions. For comparison, instrument noise on the VNIR array is ~5.5 DN.

To derive radiometric calibration factors for PICARD, we make use of a spatially homogeneous illumination source in the form of ASF's 91 cm integrating sphere that contains a combination of one 100 W and eleven 35 W incandescent lamps. The peak radiant intensity at 12 lamps is about 820 W m^{-2} μm^{-1} sr^{-1} at a wavelength of 840 nm. Analog saturation effects on the VNIR detector begin to appear in some channels with more than ten 35 W lamps in the instrument configuration used for PACE-PAX, and so the 11- and 12-lamp-level images were not used for calibration.

A bright, non-saturating PICARD image of the sphere is used as the basis for the NUC after the dark level has been subtracted. We create the NUC image frames by calculating the ratio of the average response of the 412 illuminated across-track pixels in each row (band) divided by the individual response of each element in a row of the detector array for the dark-corrected bright lamp image, d_b. These NUC gain factors generally range from about 0.8 near the nadir to 1.4 or so near the edges, plus some pixel-to-pixel variation (Figure 4). Fortunately, the temperature of the SWIR optical bench has not been observed to affect the SWIR radiometric gains or the NUC image after dark subtraction.

$$N(r,c) = \left[\frac{1}{412}\sum_{c=1}^{412} d_b(r,c) - d_0(r,c)\right] / [d_b(r,c) - d_0(r,c)] \quad (6)$$

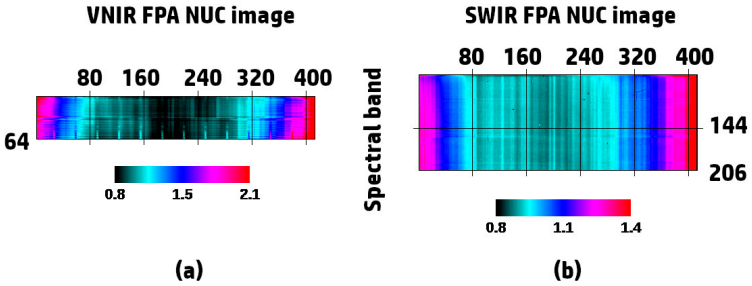

Figure 4. PICARD non-uniformity correction (NUC) images for the VNIR FPA (**a**) and SWIR FPA (**b**) derived from ASF integrating sphere imagery collected prior to PACE-PAX. The illuminated 412 across-track pixels are shown for each detector array. NUC values are a unitless ratio of the cross-track average response to the individual pixel responses over the sphere.

A bad pixel mask gets created from 0-lamp sphere measurements that identify outlier pixels on each detector array and is applied following the NUC by interpolating bad pixel values based on neighboring good pixel values. To derive the bad pixel mask, we calculate a quadratic fit of the across-track response averaged over a few hundred 0-lamp frames. The standard errors for each fit line can be estimated. If E is the standard error of the polynomial fit for each spectral row and k is a user-defined threshold factor, then the bad pixel mask can be extracted when the absolute difference between the mean zero-point response, d_0(r,c), and the fit is over the defined threshold standard error. That is,

$$| d_0(r, c) - F(r, c) | > E(r) \cdot k, \quad (7)$$

where F(r, c) is the across-track quadratic fit value for pixel (r, c). Using the absolute difference identifies both hot and cold pixels. Currently we have set the threshold factor values for VNIR and SWIR to 2.8 and 2.5, respectively.

Finally, we use the corrected responses at each lamp level to fit the linear model described by Equation (4) based on a series of integrating sphere lamp levels up to 10 lamps. The observed radiance for each spectral band is estimated by convolving a Gaussian function of specified band center and FWHM with the FEL-to-OL750-based spectral radiance measurements for each lamp level. The radiometric calibration gains are then simply provided by a linear regression to calculate the slopes of observed radiance versus average corrected PICARD response. These gains then get multiplied by corrected PICARD responses recorded during flight to recover spectral radiance. The standard error of the slope estimates also serves as an estimate of sensor radiometric stability, with VNIR stability over the sphere contributing <1% uncertainty and SWIR stability contributing <0.25% uncertainty.

2.5. Spectral Stray Light Correction

For a PICARD measured response vector, y_{meas}, of dimension n equal to the number of spectral channels for the instrument, we want to split out the in-band and stray light response components, y_{IB} and y_{SL}. The GLAMR measurements of the instrument SRFs can be arranged in an m × n matrix, Q, where m is much greater than n. Likewise, the Gaussian fits and the stray light residuals can be arranged into m × n matrices, R and S, respectively. We define the stray light distribution functions (SDFs) to be the residual responsivity, S, after subtracting the Gaussian fits from the measured SRFs.

$$S = Q - R \tag{8}$$

Normalizing the Gaussian fits, R, by their peak values allows us to arrange them into an m × n resampling matrix, H, that we use to define reduced-dimension square n × n matrices as follows.

$$R' = H^T \cdot R \tag{9}$$

$$S' = H^T \cdot S \tag{10}$$

Each row of these matrices corresponds to one of PICARD's spectral bins, and each column corresponds to an excitation wavelength equal to the center wavelength of one of the Gaussian fits for a PICARD SRF. This process is discussed in more detail in Section 4.1 and is illustrated by Figure 5 for PICARD channel 05 in the VNIR.

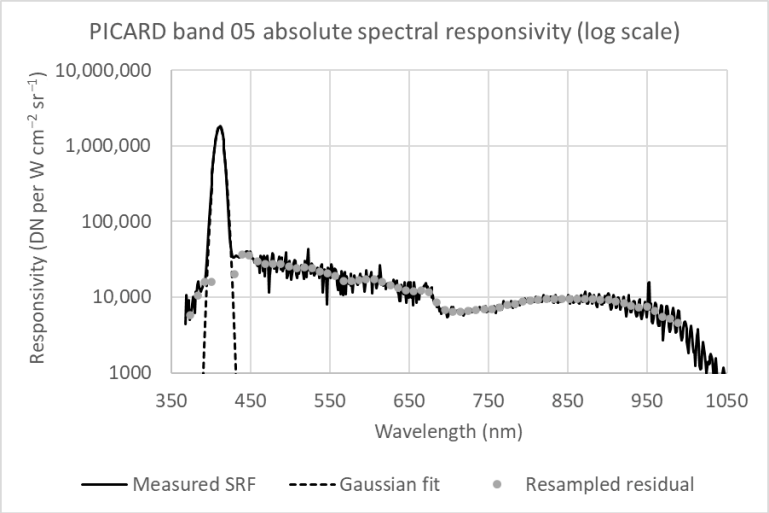

Figure 5. PICARD band 05 observed SRF, Gaussian fit SRF, and stray light residual after dimensionality reduction by resampling to PICARD VNIR bands.

The reduced-dimension SDF matrix, S′, forms the basis of the stray light correction matrix, following the procedure laid out by [14]. We use the column-wise (by excitation wavelength) summation of the reduced-dimension Gaussian fits to normalize the reduced-dimension SDF by column, with results corresponding to the D matrix defined in [14]. For each excitation wavelength, j, we calculate the in-band column response vector, s, to be

$$s[j] = \sum_{i=1}^{n} R'[i,j] \tag{11}$$

and then

$$D[i,j] = S'[i,j]/s[j] \tag{12}$$

Adding D to the diagonal identity gives us another matrix, A, that can be inverted to give us a correction matrix, C. This correction matrix gets applied to the PICARD measured response vector to recover the estimate of in-band response and reduce the stray light contamination. We also use these matrices to recover an estimate of stray light response. The in-band response then gets multiplied by the in-band radiometric gain vector, G_{IB}, to recover the in-band radiance. We use the same gains to express the stray light response in radiance units.

$$y_{IB} = C \cdot y_{meas} \quad (13)$$

$$y_{SL} = D \cdot C \cdot y_{meas} \quad (14)$$

$$L_{IB}(r, c) = G_{IB}(r) \cdot y_{IB}(r, c) \quad (15)$$

$$L_{SL}(r, c) = G_{IB}(r) \cdot y_{SL}(r, c) \quad (16)$$

The correction matrix, C, is applied to laboratory calibration imagery over the sphere to derive in-band calibration gains, G_{IB}, that are only applicable to PICARD imagery that has also had the stray light correction applied. In the next section, these in-band calibration gains derived from an incandescent laboratory source are shown to provide accurate estimates of absolute radiance under solar illumination, in contrast to calibration gains derived without accounting for spectral stray light.

3. Results

Radiance values derived from ground and satellite measurements were used as validation references for the PICARD laboratory calibration at altitude. Since 2013, the NASA ER-2 program has flown the Western Diversity Time Series survey (WDTS) [26] to study the landscapes of California and Nevada, with ASF's MASTER providing longwave and thermal infrared imaging in 25 channels covering 3–12 μm wavelength radiation and JPL's Airborne Visible/Infrared Imaging Spectrometer (AVIRIS-Classic) providing hyperspectral imagery in the 0.4 to 2.5 μm range [27]. The NASA ER-2 "space plane" is the civilian variant of the Lockheed U-2 reconnaissance aircraft that flies airborne science missions at 20 km (65,000 ft) above sea level [28]. PICARD operates within the forebody of the instrument "superpod" underneath either wing connected to an independent Inertial Measurement Unit (IMU) on the instrument and Global Positioning System (GPS) antenna mounted on the pod roof.

In March through May of 2023, PICARD participated in the annual WDTS campaign with a secondary flight request to obtain validation imagery over thick banks of marine stratus clouds in coordination with satellite overpasses by Terra, Aqua and NOAA-20. An additional flight on a clear day over Railroad Valley, Nevada, allowed comparison between PICARD airborne imagery and modeled at-sensor radiances derived from automated ground measurements at a stationary site on the dry lakebed. Railroad Valley was also used as a validation target for PICARD during PACE-PAX in September 2024. In the following sections, we will show the comparison results using the original PICARD calibration method without the benefit of stray light correction and then the updated comparison using calibrations that incorporate the stray light correction resulting from the GLAMR experiment in February 2024.

3.1. Comparison to Ground Radiance

At-sensor radiance values based on ground measurements on the dry lakebed were provided by the Radiometric Calibration Network (RadCalNet) Working Group [29], an international collaboration among multiple institutions, developed and operated by the CEOS (Committee on Earth Observation Satellites) Working Group on Calibration & Val-

idation (WGCV) for the calibration and validation of Earth-observing sensors. The US Geological Survey (USGS) maintains an automated RadCalNet measurement site at the Railroad Valley dry lakebed, or playa, located at 38.5°N, 115.7°W in central Nevada [15]. Railroad Valley (RRV) has served as a vicarious radiometric calibration and validation target for many Earth-observing sensors, including those on Landsat 8 and 9, MODIS, and VIIRS [30]. It is a critical site for sensor intercomparison and cross-calibration activities due to its spatially and spectrally smooth surface of compacted clay minerals and typically clean, dry atmosphere [31,32]. The RadCalNet provides consistent top-of-atmosphere (TOA) spectrally resolved reflectance products over several sites around the world and specially provided ASF with modeled at-sensor radiance values for ER-2 altitudes (20 km).

Four passes with PICARD over the USGS RadCalNet at RRV were flown on 2 May 2023 at 15 to 20 min intervals. An example PICARD image of Railroad Valley is shown in Figure 6. Four additional passes over RRV were flown on three separate flights during PACE-PAX in September 2024. The high-resolution at-sensor radiance spectra provided to ASF by RadCalNet for the times of PICARD overflights of RRV playa were resampled from 1 nm spacing to match the PICARD SRFs spaced roughly 10 nm apart. The playa radiance represents a 1 km^2 region, and so we averaged together the responses of a 30-by-30-pixel region of the 33 m gridded PICARD imagery for the comparison to RadCalNet. Figure 7 shows this comparison to the playa for the original PICARD calibration without the GLAMR-based stray light correction together with the comparisons to satellite imagery of marine stratus clouds discussed next.

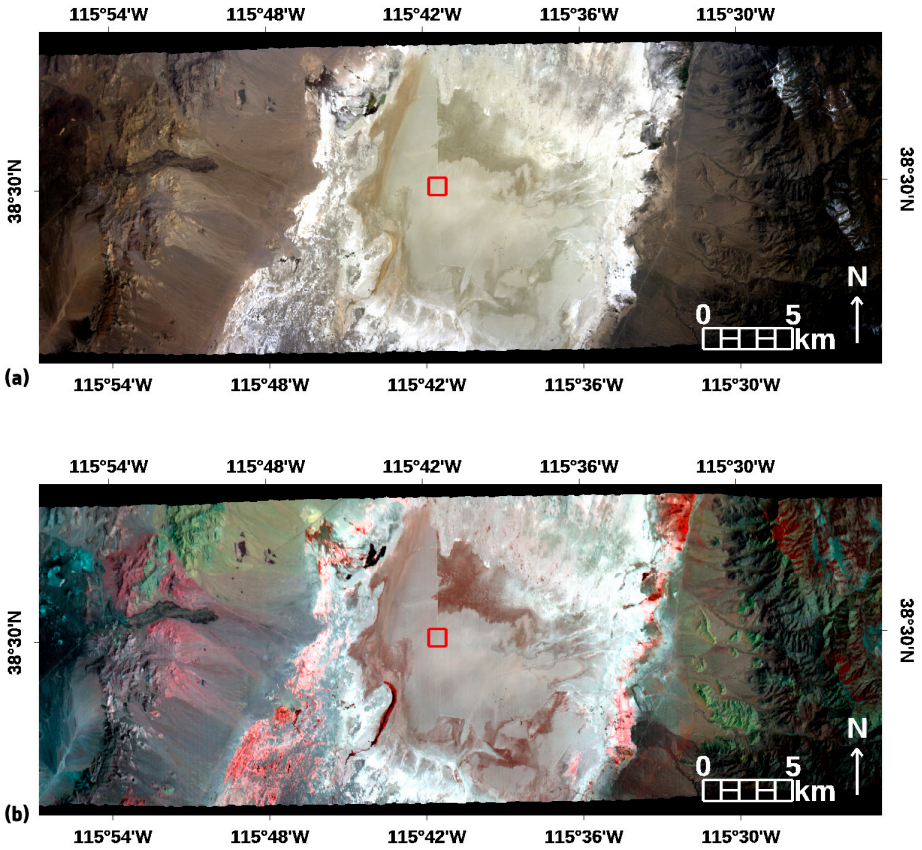

Figure 6. PICARD 33 m geospatially gridded image of Railroad Valley (RRV) dry lakebed in central Nevada, collected 2 May 2023, in true color using bands at 0.66 µm, 0.56 µm, and 0.46 µm (**a**) and false-color infrared using bands at 1.02 µm, 2.20 µm, and 2.34 µm (**b**) for red, green, and blue (RGB) color channels. Red square outlines the RadCalNet region of interest centered at 38.5°N, 115.69°W.

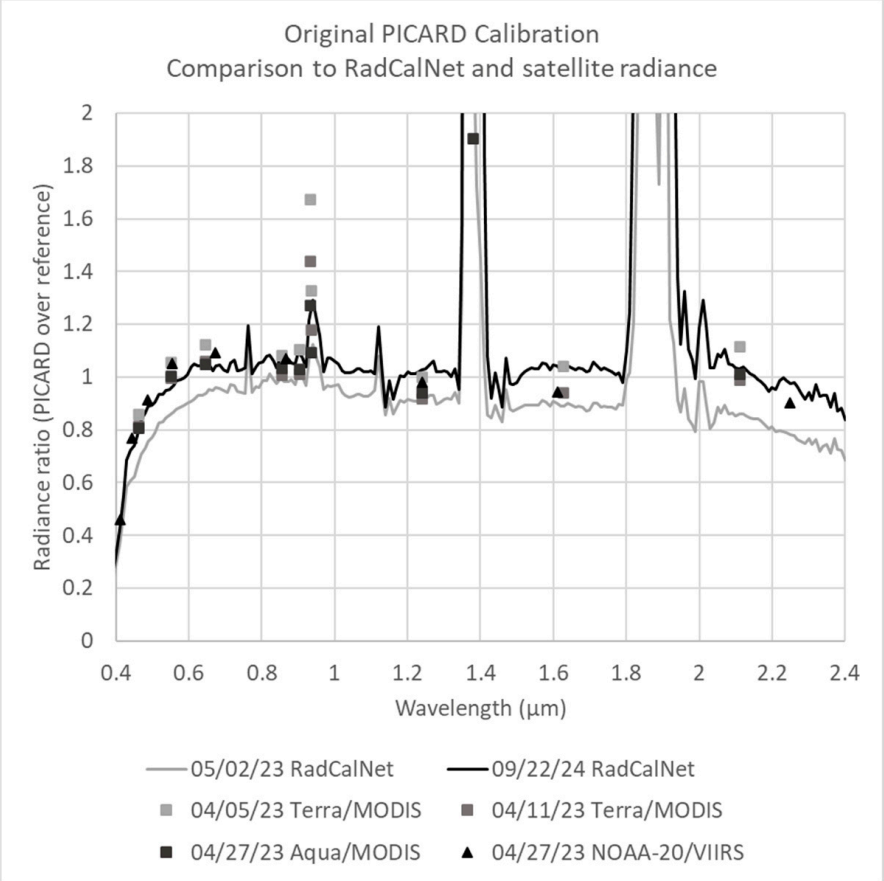

Figure 7. Comparison of PICARD radiance measurements without GLAMR stray light correction to USGS RadCalNet modeled at-sensor radiance for Railroad Valley (RRV) playa and satellite radiance measurements of marine stratus clouds coincident with ER-2 PICARD validation flights for Terra MODIS, Aqua MODIS, and NOAA-20 VIIRS imagery. Ratios were calculated on a pixel-by-pixel and band-by-band basis from pseudo-satellite imagery generated from higher-resolution PICARD imagery when compared to satellites.

3.2. Comparison to Satellite Radiance

Relatively homogeneous layers of marine stratocumulus clouds over open ocean have been previously used as targets for radiometric comparisons against satellite measurements, for example, in [33,34], and so the ER-2 could fly validation flights for PICARD in coordination with satellite overpasses when the clear skies necessary for WDTS objectives were unavailable. Due to careful flight planning and excellent pilot skill, the PICARD nadir aligned quite closely to the satellite nadir, making it straightforward to align sensor viewing angles. Airborne imagery collected while flying at 20 km (65,000 ft) altitude along the satellite flight path at the time of overpass can be directly compared to the satellite imagery, with both sensors viewing the same clouds at nearly the same time and angle. PICARD was flown in coordination with Terra MODIS on 5 April and 11 April 2023 and then in coordination with both Aqua MODIS and NOAA-20 VIIRS on 27 April. An example PICARD SWIR image of marine stratus clouds over the Santa Barbara Channel is shown in comparison to MODIS imagery from 11 April 2023 in Figure 8. The magenta region of interest superimposed over the MODIS image corresponds to the PICARD sensor zenith 5° cutoff used for the comparison. This entire region corresponds to MODIS sensor zenith angles less than 1°.

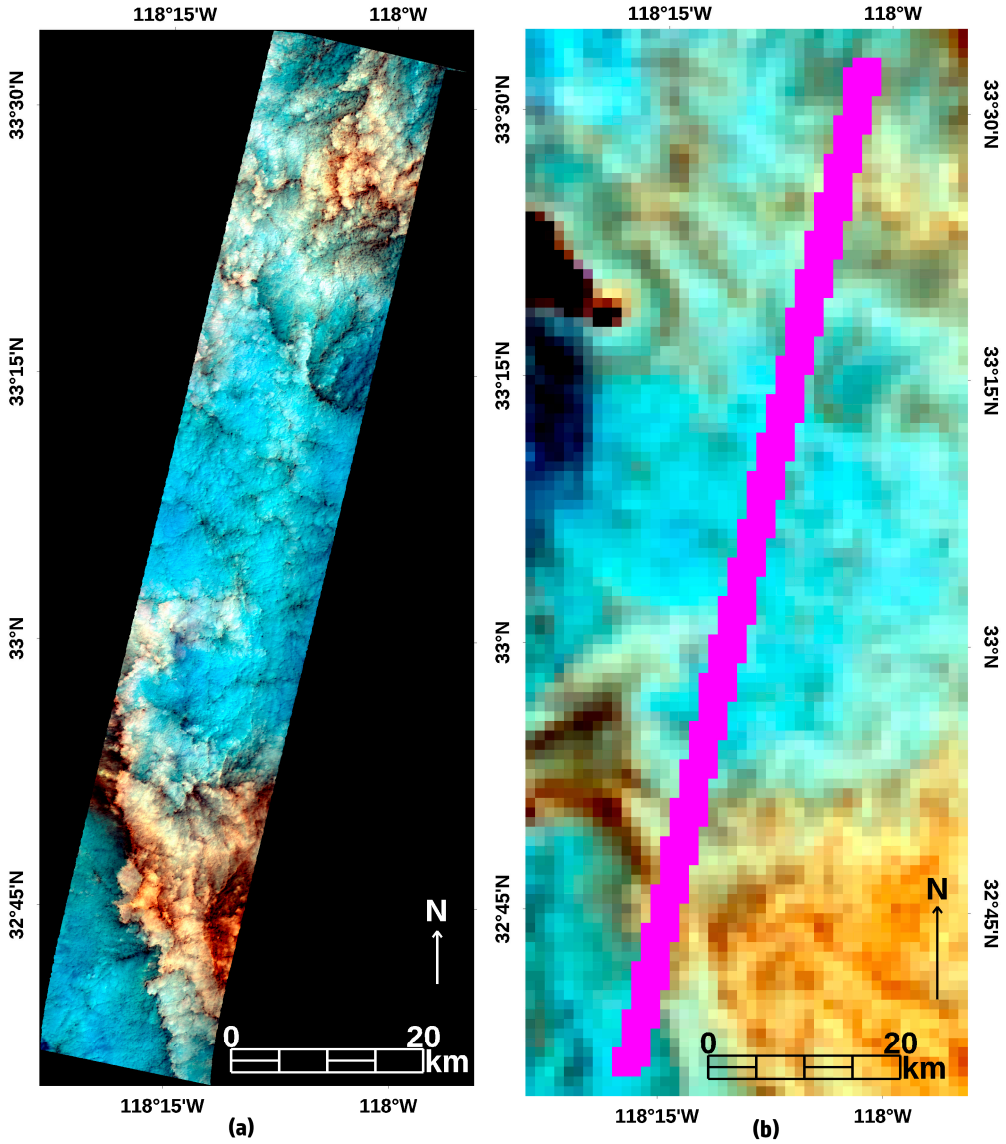

Figure 8. PICARD 33 m imagery (**a**) collected 11 April 2023 at ~18:20 UTC compared to simultaneous Terra MODIS 1 km imagery (**b**) of marine stratus clouds over Santa Barbara Channel at 33N, 118W. The red, green, and blue (RGB) color channels of these images are mapped to the 2.12 μm, 1.60 μm, and 1.24 μm spectral bands for MODIS and PICARD, vibrantly highlighting changes in cloud scattering properties due to differences in droplet size. The magenta region of interest superimposed on MODIS imagery corresponds to a PICARD zenith sensor zenith angle less than 5° and a MODIS sensor zenith angle less than 1° used for radiance ratio calculations.

To directly compare PICARD radiance measurements to satellite radiance measurements, we created pseudo-satellite imagery from the airborne data by averaging together several spatial pixels and spectral bands, thereby resampling the higher-spatial and -spectral-resolution airborne PICARD imagery to match the coarser satellite resolutions. For the spectral resampling, we convolved the broadband satellite SRFs with the narrow-band PICARD measurements. The spatial matching was accomplished by first gridding the geolocated PICARD measurements to a 33 m geographic interval, convolving the result with a Gaussian low-pass filter with FWHM roughly matching the satellite resolution to reduce high-frequency artifacts from aliasing, and then re-gridding the convolution results to match the coarser spatial gridding of the satellite imagery. Radiance ratios for PICARD sensor zenith angles less than 5 degrees were then calculated pixel by pixel and band by band for imagery collected within 10 min of each satellite overpass. Figure 8 depicts

this region of interest for the Terra overpass on 11 April in magenta superimposed on the MODIS cloud imagery. High cirrus clouds present in any of the imagery near the time of satellite overpass were identified using the PICARD 1.38 µm water absorption channel (band 104) and excluded from this analysis. Figure 9 shows all the PICARD resampled 1 km pixel (or 750 m for VIIRS) pseudo-satellite imagery created for these comparisons next to the actual satellite imagery of the same regions on the Earth's surface at the time of PICARD data collection.

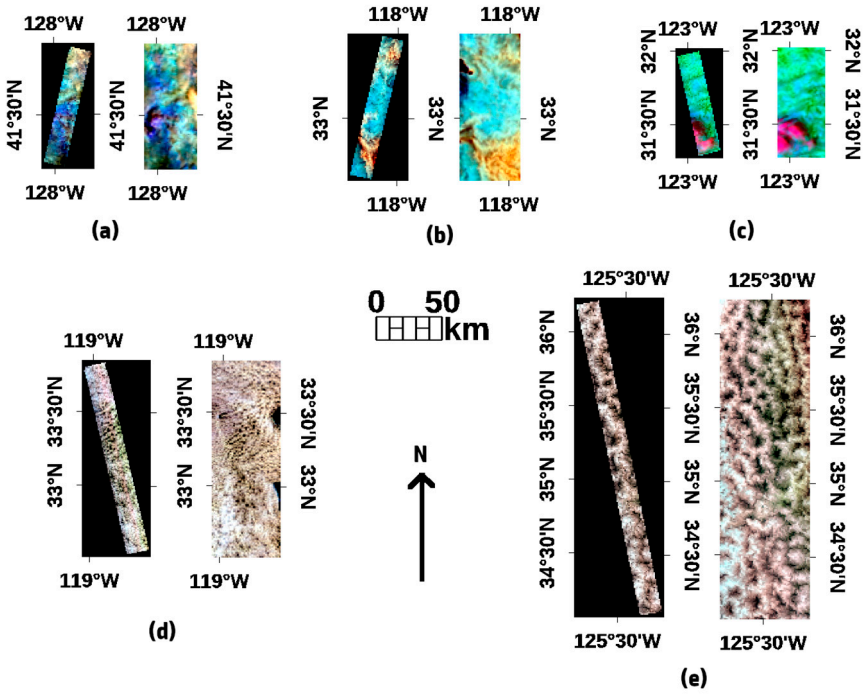

Figure 9. The left side of each image pair shows the pseudo-satellite imagery created by resampling PICARD airborne imagery to match the 1 km (MODIS and OCI) or 750 m (VIIRS) gridded pixel size of the satellite imagery, together with the actual satellite imagery used for these comparisons (right side of each image pair): (**a**) Terra MODIS 4/5/23; (**b**) Terra MODIS 4/11/23; (**c**) Aqua MODIS 4/27/23; (**d**) NOAA-20 VIIRS 4/27/23; (**e**) PACE-OCI 9/4/24. All images shown except the Aqua MODIS pair are false-color images using SWIR bands at 2.1 µm (MODIS) or 2.25 µm (VIIRS and OCI), 1.6 µm, and 1.24 µm wavelengths for RGB color channels. The Aqua MODIS pair (**c**) uses SWIR bands at 1.38 µm, 2.1 µm, and 1.24 µm for RGB to highlight the high cirrus cloud bank in the lower left region of the image that was excluded from the comparison. The PICARD flight path was closely aligned with the satellite nadir in all cases.

The mean values for the ratio of PICARD radiance without stray light correction to reference satellite imagery are shown in Figure 7, and the standard deviations of the ratios are shown together with the means in Table 2. The comparison of PICARD to Railroad Valley RadCalNet radiance is also summarized in Table 2, resampled to VIIRS SRFs. A small number of passes over the playa are not enough to generate meaningful statistics, whereas the satellite comparisons provide dozens to hundreds of individual pixel samples along the ER-2 flight path for generating a robust statistical comparison between PICARD and the satellite imagers. The difference between a pseudo-satellite pixel and an actual satellite pixel is constituted by a combination of factors, including the radiometric uncertainties of both sensors (the number of photons counted) and the geometric uncertainties of each sensor (where the instrument is looking and at what angle). Moreover, clouds move and there may be significant breaks in the cloud layer, resulting in spatiotemporal heterogeneity that contributes to the variance when comparing many radiance measurements from two instruments, even over a narrow time window. Comparing two sensors in this fashion

therefore places an upper bound on the end-to-end uncertainty between the two systems, including geometric uncertainty. Similar comparisons between airborne and satellite systems found good agreement with a 4 to 5% difference (k = 1) between sensors [35,36].

Table 2. Ratios of PICARD radiance values without GLAMR stray light correction relative to reference measurements (means and standard deviations). Ratios were calculated on a pixel-by-pixel and band-by-band basis from pseudo-satellite imagery generated from higher-resolution PICARD imagery when compared to satellites. RadCalNet and PACE-OCI spectra were resampled to VIIRS spectral channels to summarize results in this table. Bad detectors in Aqua/MODIS band 6 and saturation over the target in VIIRS band 6 prevent comparison to PICARD data. Results in italics correspond to a significant atmospheric absorption feature at 0.935 μm and a major absorption feature at 1.38 μm.

MODIS	Center	Terra MODIS 4/5/23		Terra MODIS 4/11/23		Aqua MODIS 4/27/23	
Band No.	Wvl (μm)	Mean	StDev	Mean	StDev	Mean	StDev
3	0.464	0.858	0.046	0.815	0.031	0.807	0.043
4	0.552	1.055	0.062	0.996	0.043	1.004	0.061
1	0.645	1.122	0.067	1.057	0.047	1.049	0.069
2	0.855	1.082	0.066	1.009	0.046	1.034	0.071
17	0.903	1.103	0.073	1.011	0.047	1.029	0.071
18	*0.934*	*1.674*	*0.157*	*1.437*	*0.070*	*1.272*	*0.084*
19	*0.935*	*1.328*	*0.104*	*1.178*	*0.054*	*1.093*	*0.073*
5	1.241	0.998	0.063	0.918	0.038	0.941	0.071
26	*1.381*	*2.099*	*0.402*	*5.757*	*1.161*	*1.902*	*0.269*
6	1.628	1.042	0.084	0.940	0.032	N/A	N/A
7	2.111	1.115	0.153	0.987	0.041	1.012	0.049
VIIRS	**Center**	**NOAA-20 VIIRS 4/27/23**		**RadCalNet RRV**		**PACE-OCI 9/4/24**	
				5/2/23	**9/24/24**		
Band No.	**Wvl (μm)**	**Mean**	**StDev**	**Value**	**Value**	**Mean**	**StDev**
1	0.412	0.459	0.033	0.386	0.443	0.397	0.022
2	0.445	0.769	0.062	0.620	0.738	0.703	0.043
3	0.488	0.915	0.081	0.746	0.878	0.843	0.058
4	0.555	1.052	0.105	0.860	0.959	0.954	0.074
5	0.672	1.092	0.121	0.950	1.029	1.013	0.087
6	0.746	N/A	N/A	0.929	1.013	0.973	0.087
7	0.865	1.071	0.124	0.984	1.057	0.986	0.090
8	1.240	0.981	0.114	0.905	1.019	1.002	0.097
9	*1.378*	*5.717*	*0.755*	*2.546*	*10.110*	*2.443*	*0.478*
10	1.610	0.944	0.101	0.897	1.037	0.956	0.085
11	2.250	0.901	0.085	0.776	0.972	0.870	0.070

3.3. Updated Comparisons to Ground and Satellite Radiance

Calibrating PICARD with the stray light correction based on the GLAMR measurements greatly improves the comparison of PICARD radiance measurements to RadCalNet and satellite data. Compare Figure 7 and Table 2 to the updated ratios shown in Figure 10 and Table 3, where the blue channels of PICARD agree well with the RadCalNet and satellite reference measurements. The O_2 spike at 760 nm has disappeared with the corrected calibration, and we generally observe better agreement in atmospheric absorption features, although substantial uncertainties remain in both the PICARD measurements and RadCalNet at-sensor radiance values for these wavelength regions.

A comparison of PICARD reflectance measurements to OCI imagery of marine stratus clouds from 4 September 2024 is shown in Figure 11. Here, the ER-2 flight track and heading were aligned with the nadir orbital track and heading of the PACE observatory. PICARD radiance measurements were converted to reflectance based on solar geometry and assuming the TSIS solar spectral irradiance model for this comparison [37]. The mean and standard deviation reflectance values were calculated for a strip of imagery centered

on the exact coincidence between the ER-2 and the PACE observatory +/− roughly 2 min along track; the OCI across-track swath was limited to the width of the PICARD swath, or roughly 18.5 km (+/− 9 OCI pixels around nadir). The PICARD pseudo-satellite and OCI satellite imagery for this comparison is shown in the bottom right of Figure 9, and the pixel-by-pixel ratios before and after the GLAMR-based stray light correction are shown in Tables 2 and 3, summarized using VIIRS wavelengths.

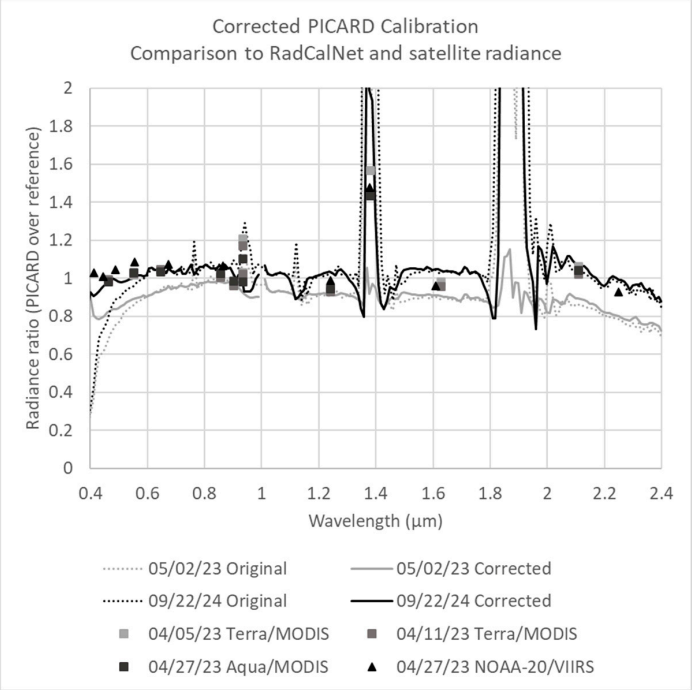

Figure 10. Comparison of PICARD radiance measurements with GLAMR stray light correction to USGS RadCalNet modeled at-sensor radiance for Railroad Valley (RRV) playa and satellite radiance measurements of marine stratus clouds coincident with ER-2 PICARD validation flights for Terra MODIS, Aqua MODIS, and NOAA-20 VIIRS imagery. Ratios were calculated on a pixel-by-pixel and band-by-band basis from simulated satellite imagery generated from higher-resolution PICARD imagery when compared to satellites.

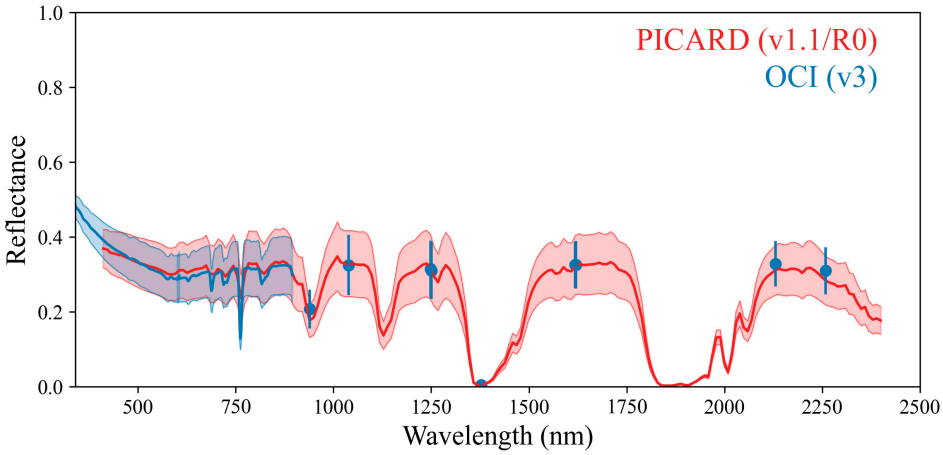

Figure 11. Comparison of PICARD at-sensor reflectance to OCI satellite measurements of marine stratus clouds on 4 September 2024. PICARD reflectance calculations were based on radiance measurements and converted using the TSIS solar model [37]. Means and 1 standard deviation error bars are shown for a strip of cloud imagery corresponding to a PICARD sensor zenith less than 5 degrees and within 2 min of the PACE satellite overpass.

Table 3. Ratios of PICARD radiance values with GLAMR stray light correction relative to reference measurements (means and standard deviations). Ratios were calculated on a pixel-by-pixel and band-by-band basis from pseudo-satellite imagery generated from higher-resolution PICARD imagery when compared to satellites. RadCalNet and PACE-OCI spectra were resampled to VIIRS spectral channels to summarize the results in this table. Bad detectors in Aqua/MODIS band 6 and saturation over the target in VIIRS band 6 prevent comparison to PICARD data. Results in italics correspond to a significant atmospheric absorption feature at 0.935 μm and a major absorption feature at 1.38 μm.

MODIS	Center	Terra MODIS 4/5/23		Terra MODIS 4/11/23		Aqua MODIS 4/27/23	
Band No.	Wvl (μm)	Mean	StDev	Mean	StDev	Mean	StDev
3	0.464	0.983	0.052	0.992	0.037	0.981	0.039
4	0.552	1.019	0.060	1.025	0.044	1.030	0.047
1	0.645	1.044	0.062	1.044	0.047	1.032	0.052
2	0.855	1.008	0.062	1.003	0.046	1.024	0.053
17	0.903	0.966	0.064	0.962	0.044	0.985	0.052
18	*0.934*	*1.205*	*0.111*	*1.171*	*0.058*	*1.102*	*0.055*
19	*0.935*	*1.031*	*0.081*	*1.019*	*0.047*	*0.982*	*0.049*
5	1.241	0.934	0.059	0.927	0.038	0.945	0.057
26	*1.381*	*1.569*	*0.301*	*3.397*	*0.684*	*1.435*	*0.181*
6	1.628	0.979	0.079	0.956	0.032	N/A	N/A
7	2.111	1.062	0.147	1.021	0.043	1.042	0.035

VIIRS	Center	NOAA-20 VIIRS 4/27/23		RadCalNet RRV 5/2/23	RadCalNet RRV 9/24/24	PACE-OCI 9/4/24	
Band No.	Wvl (μm)	Mean	StDev	Value	Value	Mean	StDev
1	0.412	1.031	0.071	0.800	0.883	0.876	0.042
2	0.445	1.010	0.080	0.795	0.954	0.936	0.055
3	0.488	1.044	0.093	0.841	0.995	0.969	0.066
4	0.555	1.084	0.108	0.890	0.998	0.984	0.076
5	0.672	1.075	0.119	0.943	1.032	1.002	0.086
6	0.746	N/A	N/A	0.934	1.020	0.972	0.087
7	0.865	1.064	0.124	0.977	1.057	0.981	0.090
8	1.240	0.990	0.115	0.912	1.023	1.011	0.097
9	*1.378*	*1.479*	*0.225*	*0.977*	*2.242*	*1.215*	*0.111*
10	1.610	0.959	0.102	0.911	1.048	0.971	0.086
11	2.250	0.927	0.087	0.796	0.989	0.907	0.072

4. Discussion

4.1. Stray Light Correction

We use the term "spectral stray light" as a catch-all for unwanted out-of-band light reaching a given detector spectral bin: reflected light from other diffraction orders, whether scattering diffusely off baffles or due to second-order harmonic effects; grating scatter due to microroughness or imperfections in the grating itself; and ghost reflections from partially reflective windows [38]. Spatial stray light from the PICARD optics and detector crosstalk was below detection limits with the MFC, and the GLAMR experimental design provides data that cannot be used to characterize spatial stray light without additional baffling. We have only characterized PICARD stray light in the spectral dimension at this time. Spectral stray light is present in all grating spectrometers and is difficult to measure with grating-based calibration sources, such as a monochromator, that themselves emit out-of-band light. The result of this spectral stray light is a discrepancy between illumination conditions in the laboratory versus in the field. The incandescent lamps we use in our integrating sphere have a peak radiant output at near-infrared wavelengths, which differs substantially from the peak radiant intensity of the sun in the human visible range. Extra out-of-band response in PICARD's blue/UV channels from infrared photons during our laboratory measurements skews our estimate of the radiometric calibration gains, and so

PICARD appeared to underreport radiance when taken into natural illumination conditions prior to the GLAMR-based stray light correction. Similarly, extra out-of-band response in PICARD's channels at wavelengths corresponding to atmospheric water absorption features causes an overreport when we apply our uncorrected lab-derived calibration slopes to in-flight imagery. So, the GLAMR-derived spectral stray light signature explains most of the observed discrepancies in our 2023 measurements.

This effect can be readily illustrated by taking advantage of the physical units attached to the measurements of spectral response thanks to GLAMR's radiometrically calibrated photodiodes and virtually monochromatic input to the integrating sphere. These combined absolute spectroradiometric response functions can then be multiplied by a known input spectral radiance, such as the OL750 measurement of the ASF integrating sphere at a particular incandescent lamp level or modeled at-sensor radiance provided by RadCalNet. The product provides a prediction of the total spectral response for a given input radiance, which can then be integrated over a wavelength to predict the actual response of the instrument for a given channel in DN. Figure 12 shows an example of this with a comparison of sensor response to the sphere at six lamps versus the response over RRV, with greater in-band response over the playa under solar illumination and greater out-of-band response from the incandescent laboratory source.

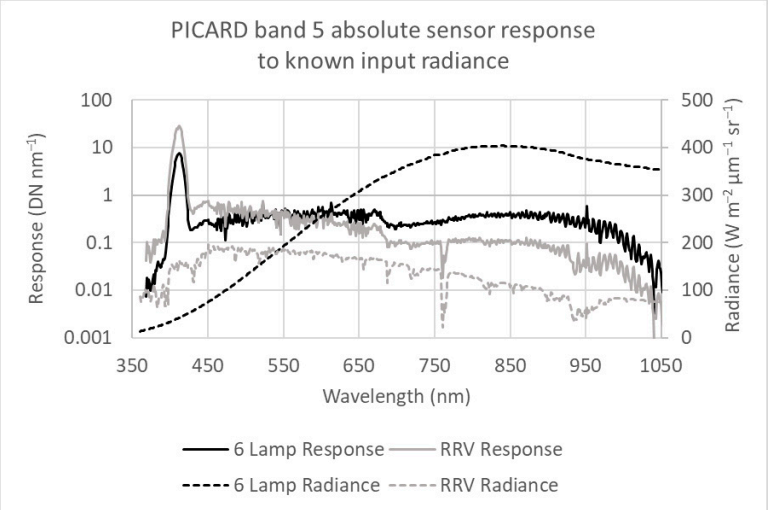

Figure 12. GLAMR measurement of PICARD SRF for channel 05 in the VNIR multiplied by OL750 radiance measurements of the ASF sphere illuminated by 6 incandescent lamps or by RadCalNet modeled at-sensor radiance of Railroad Valley (RRV) Playa imagery collected 2 May 2023, under solar illumination (using the left logarithmic *y*-axis and solid lines), along with the input radiances used for this calculation (using the right linear *y*-axis and dashed lines). A calibration based only on the primary response mode fails to capture the difference in the proportion of stray light that contributes to the total response of this channel under different illumination conditions.

The SRF for each PICARD channel must then be separated into two distinct categories: in-band and stray light. The true SRF for each band has a primary mode that is approximately Gaussian, while the remainder may be considered as stray light that should be subtracted from the measured responses to generate estimates of the desired in-band response without the spectral stray light contamination. The integral of the in-band absolute radiometric responsivity over the entire wavelength range is equal to the reciprocal of the calibration gain for the selected band. Therefore, our estimate of the PICARD calibration gains using the GLAMR absolute radiance measurements depends upon our choice of method for separating the in-band response mode from the stray light signature, and this choice also affects the stray light correction.

The in-band SRFs obtained through GLAMR may also be normalized and the stray light-corrected response may be used in combination with a broadband incandescent lamp source and integrating sphere to get another estimate of the PICARD calibration gains with a distinct radiometric calibration pathway. Ideally, calibration gains from both pathways agree to within-instrument uncertainty and allow for changes over time, but both estimates ultimately depend on the method used to separate the in-band response from the stray light.

To estimate the primary Gaussian response mode for each band, we used a least-squares Gaussian fit of the measured SRFs, a method we selected because it is widely implemented. The long tails of the stray light signature cause the fit to slightly overestimate the peak and FWHM. This results in an estimate of the stray light distribution with relatively large negative responsivity dips in the in-band region after the Gaussian mode has been subtracted from the measured SRFs (see Figure 13). For PACE-PAX, we defined the SDFs to be non-negative, clipping unphysical residual values. After PACE-PAX, we tested another method for defining the Gaussian fits with the aim of minimizing the negative residual responsivities, which is also depicted in Figure 13 and discussed in more detail shortly.

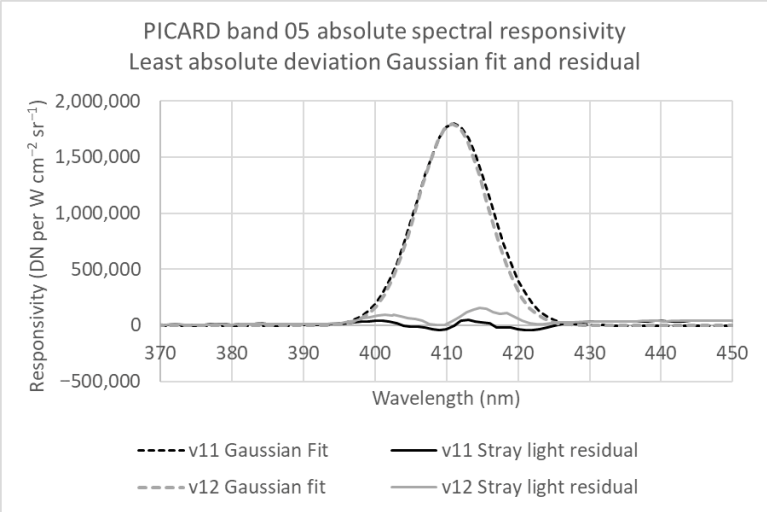

Figure 13. Example residual differences between measured GLAMR SRF for the PICARD VNIR channel 05 and the least-squares Gaussian fit of the SRF (solid black line), along with the Gaussian fit (dashed black line). The least-squares fit was used to define the v11 stray light matrix used for calibration during PACE-PAX. The grey lines depict the fit used for v12 (dashed grey line) minimizing negative residuals (solid grey line) tested after the campaign and discussed below.

Compare this approach to [14], which presented a simple spectral stray light correction method for array spectrometers. The authors used a tunable laser to excite detector pixels, sampling roughly one out of every five spectral pixels across their array and interpolating and extrapolating the results to the remaining pixels. Then they defined the in-band portion to be the three spectral pixels at or adjacent to the peak response value for a given excitation wavelength, and they defined the SDF to be zero within this region.

Also compare this approach to [39], where the authors oversampled excitation wavelengths in the spectral dimension (like our GLAMR measurements) and then fit their data to three simultaneous Gaussian functions with identical band centers but with varying peaks and widths. The primary response mode represents their estimate of the in-band portion, while the secondary and tertiary responses additively combine to represent their SDF estimate. Thus, their SDFs continue across the in-band region and even peak at the same location.

Where the authors of [14] interpolated their measurements to match the dimensionality of their instrument, the authors of [39] and the PICARD team had to reduce the dimensionality of our measurements to match our respective imagers. Physically, some scattered photons from imperfections in the diffraction grating are expected to match the wavelength of correctly diffracted in-band photons. Ref. [39] noted that the SDFs should therefore be continuous across the in-band region of each channel, but for the PICARD instrument one or two additional Gaussians did not match our observed SDFs very well. To expedite the delivery of the PICARD data from PACE-PAX, we performed least-squares fits of our data to a single Gaussian function for each band and subtracted these from the observed SRFs to estimate our SDFs. Then we used the Gaussian fits to define a matrix for reducing the dimensionality of our observations and the derived SDFs. By thus resampling the SDFs to match the nominal spectral resolution of the instrument itself, we can characterize an arbitrary non-Gaussian SDF for each spectral bin.

The PICARD stray light distribution matrices for the VNIR and SWIR detectors are illustrated together in Figure 14, where green intensity corresponds to stray light responsivity and magenta highlights the main diagonal. In principle, a single matrix for the instrument can be calculated and applied to the spectrally merged data from both detectors. However, early design decisions for the processing software architecture made it very computationally expensive to do this with negligible changes in output radiance in our testing. Thus, we calculated and applied the correction matrices separately for each detector prior to merging. As can be seen in Figure 14, almost no stray light contamination crosses the dichroic, and so each detector array can be used to estimate the stray light response for itself without the need for information from the other detector array. The GLAMR experiment also revealed a second-order harmonic effect on the SWIR detector, where 1000 nm to 1100 nm photons induce a small secondary peak responsivity in detector bins corresponding to twice their wavelength. This secondary peak is ~0.1% of the primary peak, only making a small contribution to the total response. But the GLAMR data revealed its presence and allowed us to account for it in our measurements.

When we apply the C matrix correction to PICARD measurements of our broadband integrating sphere, we can calculate calibration coefficients that apply to airborne imagery that has also been corrected with this C matrix. These stray light-corrected coefficients differ most from the uncorrected coefficients where the uncorrected PICARD calibration differed most from the Railroad Valley RadCalNet radiance. The corrected coefficients obtained from sphere measurements in August 2024 compare well with the coefficients obtained by integrating our defined in-band Gaussian fits of the GLAMR absolute responsivities measured in February 2024 (see Figure 15).

After delivering Level 1B PICARD data for PACE-PAX, we tested another method for estimating the primary response Gaussians by minimizing the negative residual responsivity of the SDFs after subtracting the Gaussians. A human analyst manually adjusted the three parameters that define each Gaussian while graphing the residuals with the aim of avoiding unphysical negative values that were not due to noise (Figure 13). The result of this was a slightly different stray light correction matrix that subtracted more stray light response and considerably improved the agreement between calibration coefficients derived from sphere measurements versus those derived from integrating the GLAMR responsivity in the VNIR and in the SWIR above 2000 nm wavelengths. However, the output radiance values for our airborne data changed very little when using the ASF sphere for final radiometric calibration, as illustrated in comparison to the Grande broadband integrating sphere at NASA Goddard (Figure 16). Therefore, we have not yet reprocessed data from the PACE-PAX campaign for delivery to the data archive.

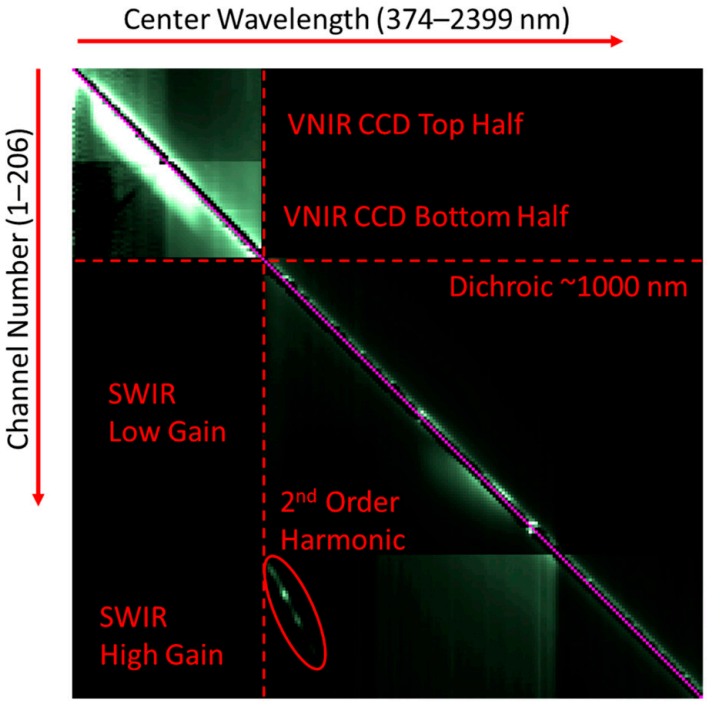

Figure 14. Visualization of PICARD's stray light distribution matrices for the VNIR and SWIR detectors. Applying a merged matrix to the data proved very computationally expensive while making negligible difference, and so in practice the matrices are calculated and applied separately for each focal-plane array. Green intensity corresponds to stray light responsivity, and magenta highlights the main diagonal. A second-order harmonic effect on the SWIR detector was observed, where 1000 to 1100 nm photons induce a small (~0.1%) secondary peak responsivity in detector bins corresponding to twice their wavelength.

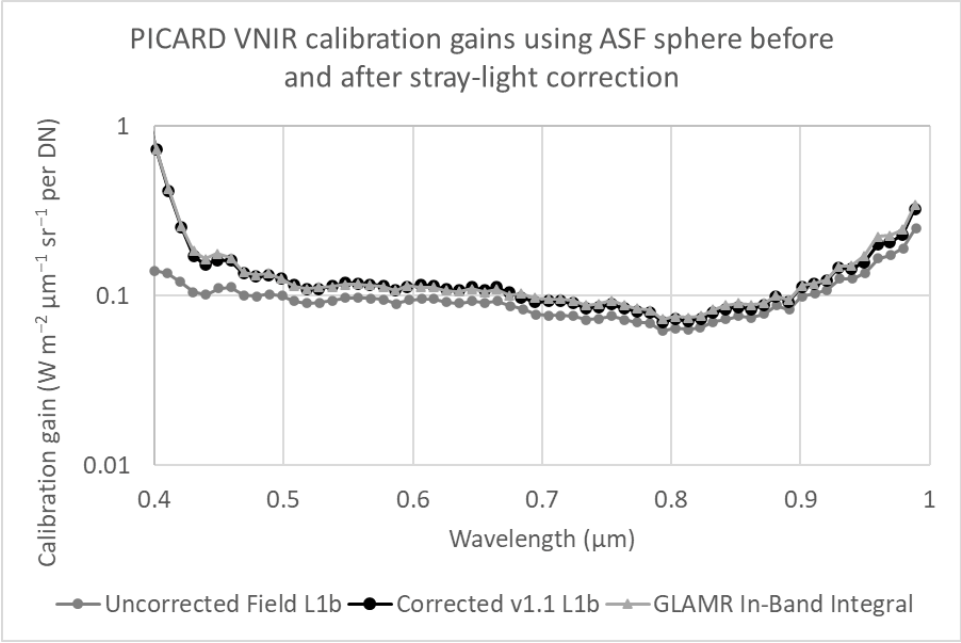

Figure 15. PICARD VNIR calibration coefficients using ASF sphere data before and after applying the stray light correction based on the GLAMR experiment compared to the coefficients derived from integrating the in-band responsivities of the PICARD SRFs measured with GLAMR.

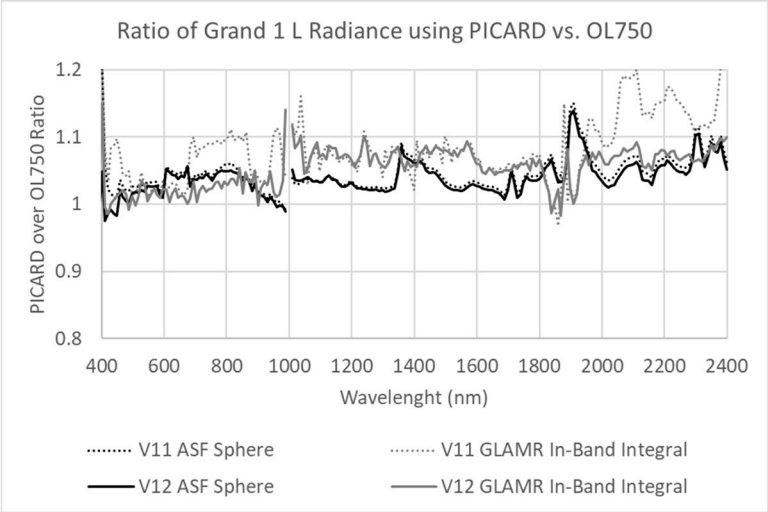

Figure 16. Comparison of radiance measurements of GSFC Grande sphere at 1 lamp using PICARD relative to OL750. Four different methods for calculating the PICARD calibration coefficients were tested using two different ways of calculating the stray light correction matrix and then either integrating the in-band SRFs using the GLAMR radiance measurements or rescaling the in-band SRFs to radiance measurements of the ASF sphere. Here, v11 and v12 refer to the matrix versions the PICARD team used during testing. The v11 matrix calculated using the least-squares Gaussian fits was used for processing PACE-PAX L1b v1.1 data, while the v12 matrix was calculated afterwards using the "minimum negative residual" method for defining the GLAMR in-band and stray light response functions.

4.2. Real-World Validation

Each pass over the RRV playa provided a single high-resolution spectrum for comparison to airborne or satellite imagery. Satellite comparisons to TOA reflectance estimates based on ground measurements of the playa at RRV [30] and Red Lake Playa, AZ [40], showed good agreement, with repeated MODIS and Landsat observations typically falling within satellite uncertainty specifications of 3 to 5% relative to TOA reflectances. The small number of passes possible during an airborne science campaign is often not enough to generate meaningful statistics, but previous comparison with eMAS to RRV demonstrated the utility of RadCalNet as a validation target for airborne sensors [41]. However, the at-sensor radiance values provided to ASF can vary by up to 10% at some wavelengths depending on the selection of ground-viewing radiometers at RRV, especially at SWIR wavelengths where eMAS observed a relatively large disagreement with RadCalnet (Figures 17 and 18). For this reason and due to the small number of samples available for comparison, ASF does not use RRV as a vicarious radiometric calibration target, only using it for validation of laboratory calibrations at altitude.

The third version of playa radiances provided to ASF for the four PICARD overpasses in 2023 resulted in the most consistent comparison, with the PICARD-to-RadCalNet ratios falling within 1% of each other at all wavelengths outside major water absorption features from pass-to-pass over changing sun angles (Figure 17). In 2024, two passes on 22 September fell within 1% of each other in comparison to the spectra provided by RadCalNet and within 5% of one pass each on 13 September and 30 September, and they also agreed well with one another at most wavelengths. However, the pass on 30 September 2024 diverged significantly in the longer SWIR wavelengths in comparison to modeled at-sensor radiance, which was likely related to the relatively low solar elevation (27°) at the time of image capture (Figure 18).

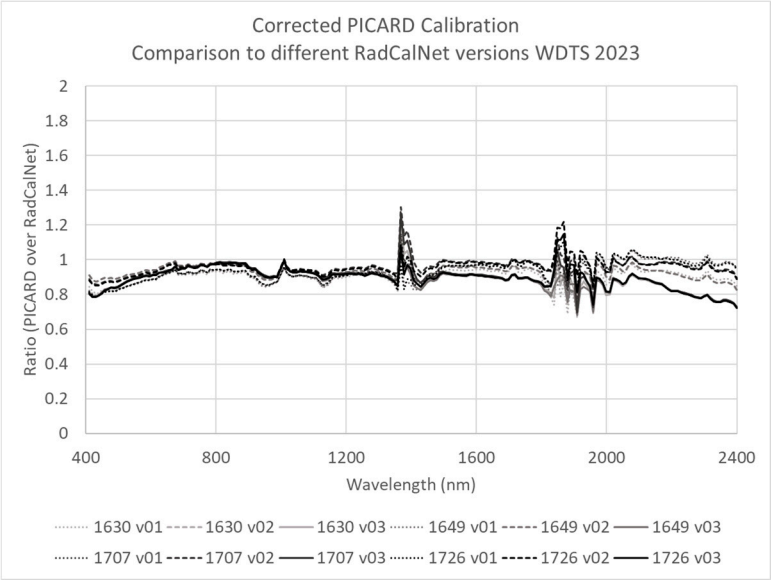

Figure 17. Ratios of PICARD measured radiance with stray light correction relative to at-sensor radiance values provided by RadCalNet for the four passes over RRV on 2 May 2023 at 1630, 1649, 1707, and 1726 UTC (light grey, grey, dark grey, and black lines). Three different versions of at-sensor radiance were provided to ASF by RadCalNet, depending on the selection of ground-viewing radiometers at the site (dotted, dashed, and solid lines).

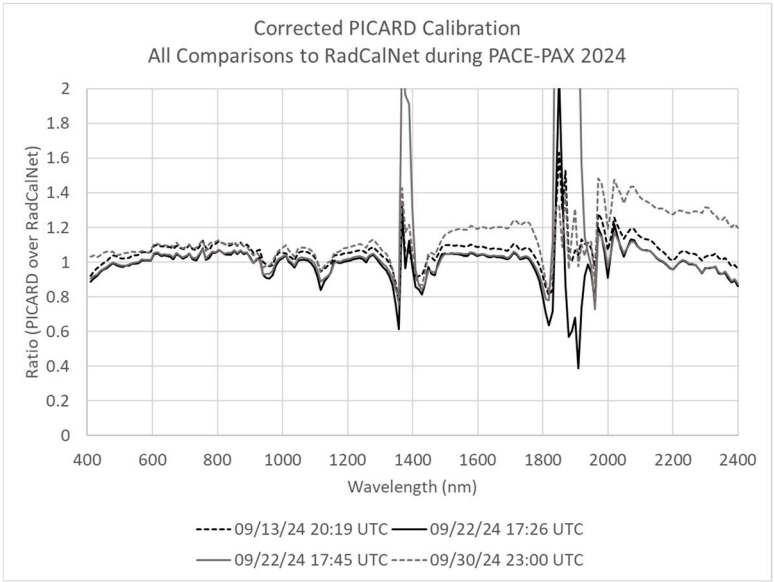

Figure 18. Ratios of PICARD measured radiance with stray light correction relative to at-sensor radiance values provided by RadCalNet for the four passes over RRV during PACE-PAX in September 2024. The low solar elevation (27°) for the pass on 30 September 2024 is likely related to the disagreement between PICARD measurements at modeled at-sensor radiance at longer wavelengths.

Significant disagreements were observed between PICARD and RRV spectra using the initial ASF laboratory calibration without GLAMR stray light correction, especially at 400 nm and below, where PICARD radiance measurements underreported by more than 70% (Figure 7). The observed spike in the ratio at 760 nm (0.76 µm) aligns with an atmospheric absorption feature due to O_2 gas, whereas the enormous five to twenty-fold PICARD overreported measurements around 1380 nm and 1900 nm correspond to major atmospheric water absorption features. Some of these discrepancies, especially in the SWIR and major water absorptions, may be due to uncertainties in the modeled

at-sensor radiance. But the magnitude of the disagreement clearly demanded further investigation, especially when the same pattern at short wavelengths was observed when directly comparing PICARD imagery to satellite imagery of marine stratus clouds.

The smoothest cloud layer observed by PICARD on 11 April 2023 was the best target for radiometric comparison. PICARD radiance measurements were typically within 3 to 5% (k = 1) of most Terra MODIS bands, with larger disagreement using the initial ASF laboratory calibration at 0.464 μm, consistent with the disagreement relative to RadCalNet at RRV (Figure 7 and Table 2). Larger spatial variability in the other scenes contributed to larger differences in comparison to VIIRS especially (Figure 9). Careful selection of smooth regions of these images by a human analyst can reduce the calculated standard deviations relative to those reported in Tables 2 and 3, which indiscriminately compare all center-swath PICARD pixels. The excellent agreement with Terra MODIS on April 11 and good agreement with other sensors over less favorable targets in 2023 demonstrated PICARD's ability to provide SWIR pseudo-satellite imagery for testing cloud and aerosol physical retrieval algorithms in readiness for PACE-PAX in September 2024. However, the satellite comparisons also confirmed the discrepancy observed relative to RadCalNet spectra at short VNIR wavelengths, prompting additional laboratory calibration measurements at ASF and later with GLAMR to understand and mitigate the disagreement.

The end-to-end uncertainty of the comparison between resampled PICARD pseudo-satellite imagery and actual satellite imagery includes the radiometric and geometric uncertainty of each instrument, as well as some movement of clouds in the scene in the short amount of time between image capture with each instrument. This analysis did not account for spatial response functions of the satellites when creating pseudo-satellite imagery and so tacitly assumed that the measured energy was distributed uniformly across the gridded pixels, which may not have been the case for scenes with significant breaks in the clouds. Table 3 presents the means and standard deviations of the updated pixel ratios. In comparison to MODIS measurements, PICARD pseudo-satellite pixel values are within a few percent on average outside atmospheric absorption features and vary by 3 to 5% (k = 1) relative to the MODIS values over the smoothest cloud scene, with larger differences over more variable scenes. Radiometric stability measurements from laboratory calibration data suggest that less than 1% of this uncertainty in the VNIR and less than 0.25% in the SWIR is attributable to PICARD radiometric instability, and repeated measurements over RRV from multiple passes in a single day are consistent with <1% PICARD radiometric uncertainty from instrument stability at altitude.

Figure 19 shows an example of how much stray light is subtracted to recover radiance estimates near or below the instrument noise floor. Applying the calibration coefficients to the standard deviation of a set of dark image frames provides an estimate of PICARD's Noise-Equivalent delta-Radiance (NEdL), the noise floor of the instrument. The NEdL shown in Figure 19 is derived from in-flight dark data to which SWIR thermal dark drift correction has been applied. The PICARD instrument temperature is controlled by an active PID control loop. When the temperature of a flightline was stable to within 0.25 C, we used the in-flight RSM dark data to correct the flightline, obtaining slightly better dark correction statistics than with the temperature fit.

Likewise, the maximum radiance measurable by the instrument in the configuration flown during PACE-PAX is calculated by applying the calibration to a response value of 10,000 DN, above which we have observed saturation effects in the VNIR detector array. The signal-to-noise ratio (SNR) depends on the input signal, but here we divide the Railroad Valley playa radiance measurements by the NEdL to provide an SNR for a moderately bright mid-latitude terrestrial target (Figure 19).

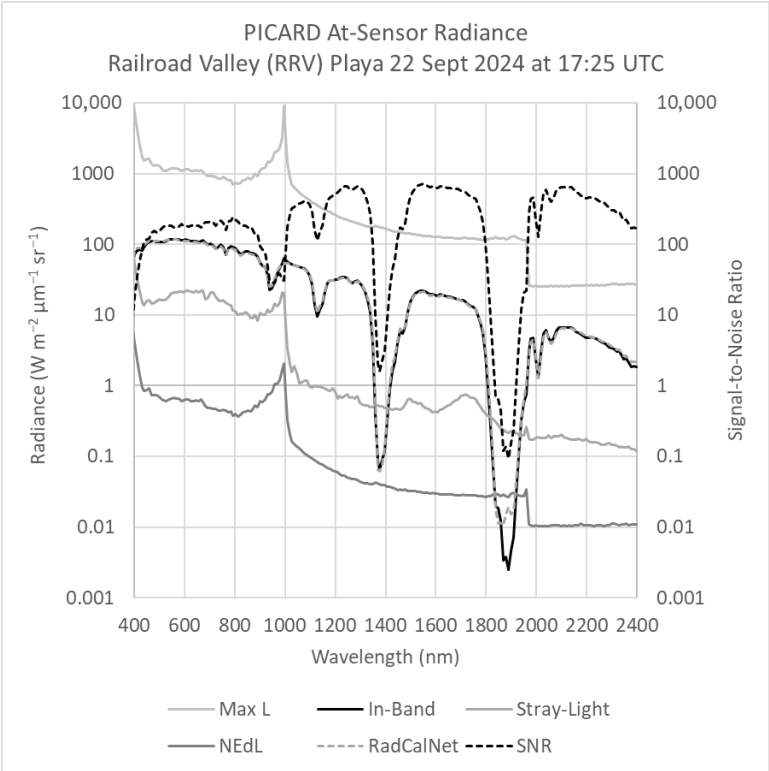

Figure 19. Maximum effective radiance (10,000 DN equivalent Max L), RRV radiances (PICARD in-band and stray light and RadCalNet reference), radiometric noise floor (NEdL), and signal-to-noise ratio (dashed SNR) for mid-latitude playa target observed through Earth's atmosphere from a 20 km altitude.

4.3. PICARD Level 1B Data for PACE-PAX

Data from the instruments that participated in the PACE-PAX campaign, including the merged PRISM/PICARD imagery, are available in Network Common Data Format version 4 (netCDF4) via open access on NASA Earthdata [42]. Each netCDF file includes the combined imagery and metadata, including timestamps, aircraft position and attitude, sensor and solar angles, and pixel geolocations for each level flight track lasting a few minutes or more. PICARD browse imagery by ER-2 flight track for the PACE-PAX campaign is available [43]. PICARD imagery from WDTS is available for download at [44], and unmerged PICARD imagery from PACE-PAX is available at [45].

Calibrated radiance imagery is stored in the netCDF files as 16-bit signed integers that must be converted to floating point radiance values by multiplying them with the CalibratedRadianceData:scale_factor included in the same file. The integer CalibratedRadianceData:band_quality flag indicates the usability of a given band for scientific purposes, with the default value of 1 indicating a well-calibrated band. The responses of the first four VNIR bands (374 to 401 nm) are heavily contaminated by stray light in the lab and field. After correction, the SNR of these channels falls close to one and the imagery is not usable. We set the band_quality flag for these channels to −99 and omitted the imagery from delivered data. The first two SWIR channels (bands 65–66 at 995 and 1002 nm) are newly characterized with the GLAMR experiment, and while they have usable imagery after stray light correction, they still require a vicarious correction factor for radiance. The band_quality flag has been set to a value of 2 for these two channels to reflect this. We suggest multiplication factors of 0.7 and 0.85 for bands 65 and 66 or devising your own vicarious correction factors before using this imagery for scientific studies. Further GLAMR measurements and refinement of the stray light correction may yield a viable lab calibration for some of the UV and new SWIR bands in future missions.

5. Conclusions

PICARD is a twin-array spectrometer that uses a dichroic mirror and two diffraction gratings to separate and sort incoming photons by wavelength before they hit the VNIR and SWIR detectors. The all-reflective telescope provides these detectors with a 49.5° field of view within a pressurized enclosure, enabling direct control of the instrument environment while aboard high-altitude aircraft. Imperfections in grating spectrometers inevitably cause a small percentage of incoming photons to scatter, resulting in spectral stray light contamination. One of the design goals for PICARD was to bring the laboratory environment to the sky, where large changes in temperature and pressure can cause changes in sensor response that can be difficult to characterize on the ground. Our experience with PICARD emphasizes the benefits of fully characterizing the spectral stray light responsivity of a grating spectrometer with a GLAMR-like setup when attempting to apply a laboratory calibration using incandescent lamps to a solar-illuminated scene.

The tunable laser light of the GLAMR experiment provided a flood of monochromatic photons across PICARD's entire field of view compared to the trickle of photons that we could produce in our lab with an incandescent source and a monochromator as input to a multi-field collimator. This gave us much greater power to explore the depths of PICARD's responsivity and allowed us to resolve the spectral stray light contamination common to grating spectrometers that had been causing the disagreement with RadCalNet and satellite radiances.

By accounting for this stray light signature in terms of PICARD's in-band spectral resolution, we can characterize an arbitrary non-Gaussian stray light distribution function for each spectral bin and apply a matrix correction to our laboratory and airborne measurements that subtracts the stray light using the method first described by [14]. The corrected calibration thus obtained provides accurate radiances independent of spectral differences between our laboratory source and solar illumination. Subtracting off the stray light also greatly improves our radiance measurements within atmospheric absorption bands when flying at high altitudes above the Earth's surface.

PICARD recently completed a case redesign enabling operation with eMAS aboard NASA's Gulfstream-III at AFRC, JSC, and LaRC [46–48]; the Gulfstream-V at JSC [49]; and King Air B200 aircraft at AFRC and LaRC [50,51], in addition to the high-altitude ER-2 [28]. The high dynamic range enabled by PICARD's dual-spectrometer design provides direct measurement of bright cloud-top radiance without saturation, but detector settings can be adjusted to provide higher SNRs over terrestrial or dark water targets, or lower SNRs and higher dynamic ranges over wildfires, and some settings can be changed between flightlines to meet multiple scientific objectives. PICARD's compact design, ease of operation, and lab-to-sky calibration are sure to be an invaluable contribution to the NASA Earth science community. Vicarious calibration methods that rely on atmospheric radiative transfer modeling continue to be vital tools for maintaining the accuracy of imagery from satellite-based sensors that cannot be recharacterized in a lab. By bringing NIST-traceable laboratory calibrations at solar reflective wavelengths to the stratosphere, PICARD provides an alternative pathway for calibrating and validating new Earth-observing sensors independent of atmospheric modeling uncertainties and offers a calibrated high-resolution test bed for physics-based algorithms that are used with weather satellite imagery to retrieve important quantities for cloud and aerosol research.

Author Contributions: G.D.H.: Conceptualization, Data curation, Formal analysis, Investigation, Methodology, Software, Validation, Visualization, Writing—original draft, Writing—review and editing. T.E.: Conceptualization, Investigation, Methodology, Software, Writing—original draft, Writing—review and editing. H.S.: Formal analysis, Methodology, Software, Validation, Writing—review and editing. A.S.: Conceptualization, Data curation, Formal analysis, Investigation, Methodology, Project administration, Visualization, Writing—review and editing. J.A.B.: Data curation, Investigation, Project administration, Resources, Writing—original draft, Writing—review and editing. R.D.: Conceptualization, Funding acquisition, Project administration, Supervision, Writing—review and editing. E.F.: Data curation, Investigation, Resources. J.J.: Conceptualization, Funding acquisition, Project administration, Resources, Supervision, Writing—review and editing. S.P.: Conceptualization, Funding acquisition, Supervision, Writing—review and editing. G.T.A.: Conceptualization, Funding acquisition, Supervision, Writing—review and editing. K.M.: Conceptualization, Data curation, Formal analysis, Funding acquisition, Software, Supervision, Visualization, Writing—review and editing. J.L.M.: Supervision, Writing—review and editing. All authors have read and agreed to the published version of the manuscript.

Funding: The development of the PICARD imager and its deployment during PACE-PAX was made possible through support from the NASA Earth Sciences Division Research and Analysis Program and the Earth Observing System (EOS) Project Science Office as part of NASA grant number 80NSSC23M0230.

Data Availability Statement: Earth-observing satellite imagery used in this study is available via open access through the NASA Earthdata portal [52], along with data from the PACE-PAX campaign, including merged PRISM/PICARD imagery [42]. Corrected PICARD imagery from WDTS 2023 is available for download at [44], and corrected PICARD imagery from PACE-PAX is available at [45]. Additional data used in this study, including uncorrected PICARD imagery and results of the GLAMR experiment, will be made available on request.

Acknowledgments: The authors thank Jeff Myers (ret.) for the initial vision that led to PICARD, the GLAMR team for our spectral calibration data, and the PACE-PAX science team for organizing a remarkably complex and successful airborne science campaign. We especially thank the ground crew, air crew, pilots, and mission management for the NASA ER-2 for their help getting PICARD airborne, and the RadCalNet team for providing at-sensor radiance values.

Conflicts of Interest: Author G. Thomas Arnold was employed by the company Science Systems and Applications Inc. Julia A. Barsi is a guest editor for this special issue. The authors declare no other conflicts of interest. The funders reviewed the manuscript as co-authors and approved the decision to publish.

Abbreviations

The following abbreviations are used in this manuscript:

NIST	National Institute for Standard and Technology
NASA	National Aeronautics and Space Administration
PICARD	Pushbroom Imagery for Cloud and Aerosol Research and Development
WDTS	Western Diversity Time Series
NOAA	National Oceanographic and Atmospheric Administration
PACE	Phytoplankton, Aerosol, Cloud, and ocean Ecosystem
PACE-PAX	PACE Postlaunch Airborne eXperiment
RadCalNet	Radiometric Calibration Network Working Group
GLAMR	Goddard Laser for Absolute Measurements of Radiance
ASF	Airborne Sensor Facility
MODIS	Moderate Resolution Imaging Spectroradiometer
ASTER	Advanced Spaceborne Thermal Emission and Reflection Radiometer
MASTER	MODIS/ASTER Airborne Simulator

eMAS	enhanced MODIS Airborne Simulator
EOS	Earth Observing System
VNIR	Visible to Near-Infrared
SWIR	Shortwave Infrared
AFRC	Armstrong Flight Research Center
OCI	Ocean Color Instrument
PRISM	Portable Remote Imaging Spectrometer
JPL	Jet Propulsion Laboratory
CIRPAS	Center for Interdisciplinary Remotely Piloted Aircraft Studies
AERONET	Aerosol Robotic Network
SI	International System of Units
ARC	Ames Research Center
GSFC	Goddard Space Flight Center
RRV	Railroad Valley
FOV	Field of View
DRB	Digital Recorder Box
POS	Position and Orientation Sensor
CCD	Charge Coupled Device
TEC	Thermo-Electric Cooler
FPA	Focal-Plane Array
MFC	Multi-Field Collimator
FWHM	Full-Width at Half-Maximum
EOSDIS	Earth Observing System Data and Information System
DN	Digital Number
NUC	Non-Uniformity Correction
RSM	Radiometric Stability Monitoring
IMU	Inertial Measurement Unit
GPS	Global Positioning System
CEOS	Committee on Earth Observation Satellites
WGCV	Working Group on Calibration and Validation
USGS	US Geological Survey
VIIRS	Visible Infrared Imaging Radiometer Suite
TOA	Top of Atmosphere
SRF	Spectral Response Function
PTFE	Polytetrafluoroethylene
UV	Ultraviolet
SDF	Stray light Distribution Function
NEdL	Noise-Equivalent delta-Radiance
PID	Proportional–Integral–Derivative
SNR	Signal-to-Noise Ratio
TSIS	Total and Spectral Solar Irradiance Sensor
netCDF	network Common Data Format
JSC	Johnson Space Center
LaRC	Langley Research Center

Appendix A

Initial Spectral Calibration of PICARD at ASF

The ASF optics lab uses broadband illumination and a grating monochromator as input to a multi-field collimator (MFC) for locally checking optical alignment and for spatial and spectral calibration of facility instruments (Figure A1). The MFC provides seven discrete beams of unknown radiance across PICARD's field of view at a series of known wavelengths to check the spectral and spatial band center and width for the seven across-track pixel locations corresponding to the beam angles (Figure A1). The MFC

can accept multiple broadband or monochromatic sources. We used a lamp-illuminated monochromator to characterize relative spectral response functions. The monochromator was calibrated using a HeNe laser as input to determine the 632.8 nm and 1265.6 nm positions. An arcsecond theodolite was used to measure the beam angles to 0.044 mRad uncertainty (k = 2).

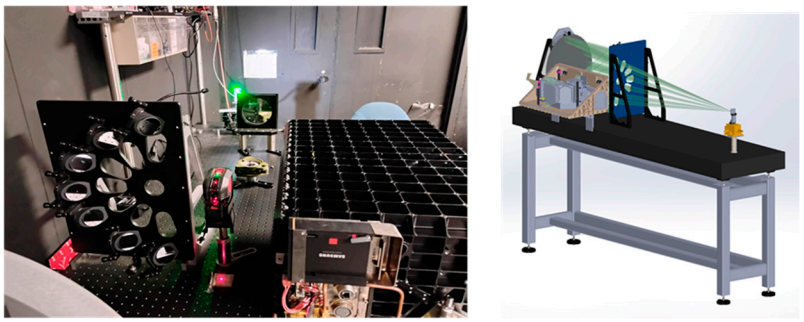

Figure A1. Photograph (**left**) and CAD visualization (**right**) of PICARD on ASF's multi-field collimator (MFC) that splits input illumination into seven beams across the instrument slit.

The spectral scan of PICARD was performed separately for the VNIR and SWIR focal-plane arrays. The VNIR array was illuminated for 2 s at each wavelength in 0.1 nm wavelength steps from 420 nm to 950 nm using a slit and grating combination with a 0.2 nm spectral bandwidth. Similarly, the SWIR array was illuminated for two seconds at each wavelength in 1 nm wavelength steps from 1100 to 2250 nm using a 0.5 nm spectral bandwidth. For selected illuminated pixels in our region of interest, we identified the maximum response value and fit a Gaussian function to the responses in a small wavelength window around the peak, taking care to keep it narrow enough to avoid secondary diffraction peaks from the slits in the function fits. Thus, only the top ~30% of the primary response mode was used for each fit. With the benefit of hindsight and GLAMR measurements, this turned out to be very conservative, and we could have used a much larger portion of the measured responses for the function fits, although with little change in results. The GLAMR experiment affirmed the ability of the MFC to provide measurements for spectral calibration and alignment of PICARD's primary response modes.

The across-track variation in the band center and full-width at half-maximum (FWHM) estimates (optical "smile", etc.) was found to be within tolerance to use the across-track mean value for each spectral bin, with less than a half pixel (5 nm) shift in band center and no measurable change in FWHM from detector nadir to edge with the MFC. A linear fit of these parameters in the spectral dimension was necessary to extrapolate the MFC measurements to the edges of the detector regions of interest (that is, all 64 binned VNIR channels from ~375 to 990 nm and 142 spectral bins from ~1000 to 2400 nm in the SWIR array).

Estimates of FWHM using MFC data were significantly lower (~30%) than estimates derived from Gaussian fits of the GLAMR SRFs. The MFC also only provides seven illuminated points across the instrument field of view compared to the flood illumination provided by GLAMR. Unlike the MFC, therefore, GLAMR measurements can be used to provide band center, FWHM, and peak responsivity estimates for every pixel in the array. For this study, we used the cross-track averages of the GLAMR SRFs, but preliminary analysis of Gaussian fits for each individual pixel show good agreement with the optical alignment measurements provided by the MFC, with less than 5 nm shift in band center from the center of each spectral row to the edge (Figure A2). However, it is unclear at this time why the MFC-based estimates of FWHM disagree with the GLAMR-based estimates and failed to capture the change in FWHM across the VNIR detector especially. ASF plans

to investigate improvements to our procedures when using the MFC with the benefit of our experience with GLAMR.

These optical alignments were performed without the benefit of planned improvements to the operator interface to provide real-time band center and FWHM estimates and so were "eye-balled" by a human optical engineer. The SWIR alignment is better than the VNIR alignment. We anticipate improvements to the optical alignment with improved software when ASF can dedicate some time to the task.

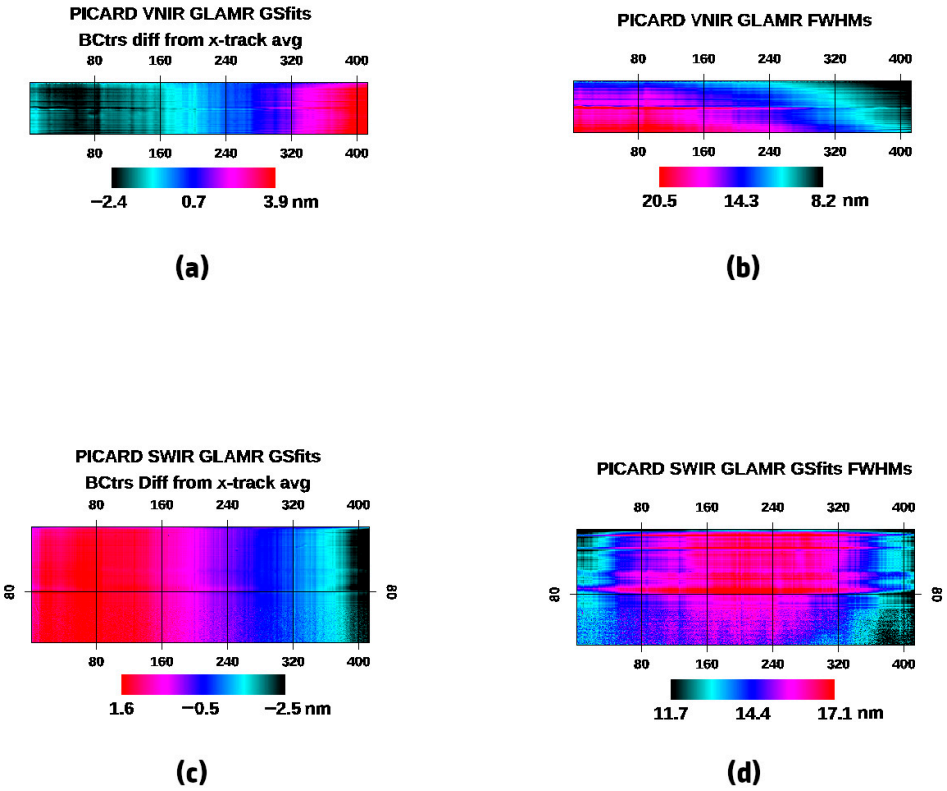

Figure A2. Preliminary analysis of Gaussian fits of GLAMR measurements for each individual pixel in PICARD's VNIR and SWIR detector arrays. The VNIR differences in band center from cross-track means (**a**), VNIR FWHM estimates (**b**), SWIR differences in band center from cross-track means (**c**), and SWIR FWHM estimates (**d**) are shown.

References

1. Hook, S.; Myers, J.; Thome, K.J.; Fitzgerald, M.; Kahle, A.B. The MODIS/ASTER airborne simulator (MASTER)—A new instrument for earth science studies. *Remote Sens. Environ.* **2001**, *76*, 93–102. [CrossRef]
2. NASA. Airborne Sensor Facility MASTER Homepage. Available online: https://asapdata.arc.nasa.gov/sensors/master/ (accessed on 4 February 2026).
3. King, M.D.; Menzel, W.P.; Grant, P.S.; Myers, J.S.; Arnold, G.T.; Platnick, S.E.; Gumley, L.E.; Tsay, S.-C.; Moeller, C.C.; Fitzgerald, M.; et al. Airborne scanning spectrometer for remote sensing of cloud, aerosol, water vapor and surface properties. *J. Atmos. Ocean. Technol.* **1996**, *13*, 777–794.
4. NASA. Airborne Sensor Facility eMAS Homepage. Available online: https://asapdata.arc.nasa.gov/emas/ (accessed on 4 February 2026).
5. NASA. Airborne Sensor Facility PICARD Homepage. Available online: https://asapdata.arc.nasa.gov/picard/index.html (accessed on 4 February 2026).
6. Knobelspiesse, K.D.; Cairns, B.; Cetinić, I.; Craig, S.; Franz, B.A.; Gao, M.; Ibriahim, A.; Mannino, A.; Sayer, A.M.; Werdell, P.J. *The PACE Postlaunch Airborne eXperiment (PACE-PAX)*; NASA PACE Technical Report Series; Report No. NASA/TM-2023-219027/Vol. 11; NASA Goddard Space Flight Center: Greenbelt, MD, USA, 2023.

7. Werdell, P.J.; Franz, B.; Poulin, C.; Allen, J.; Cairns, B.; Caplan, S.; Cetinić, I.; Craig, S.; Gao, M.; Hasekamp, O.; et al. Life after launch: A snapshot of the first six months of NASA's Plankton, Aerosol, Cloud, Ocean Ecosystem (PACE) mission. In *Proceedings of the SPIE 13192, Sensors, Systems, and Next-Generation Satellites XXVIII 131920E, Edinburgh, UK, 16–20 September 2024*; Babu, S.R., Heliere, A., Kimura, T., Eds.; SPIE: Bellingham, WA, USA, 2024. [CrossRef]
8. Caplan, S.; Huemmrich, K.F. Unveiling PACE OCI's hyperspectral terrestrial data products. *Remote Sens. Lett.* **2025**, *16*, 422–433. [CrossRef]
9. Mouroulis, P.; van Gorp, B.; Green, R.O.; Cohen, D.; Wilson, D.; Randall, D.; Rodriguez, J.; Polanco, O.; Balasubramanian, K.; Vargas, R.; et al. Design of an Airborne Portable Remote Imaging Spectrometer (PRISM) for the coastal ocean. In Proceedings of the Earth Science Technology Forum, Crystal City, VA, USA, 22 June 2010.
10. Knobelspiesse, K.D.; Cetinić, I.; LeBlanc, S.; McClain, C.R.; Werdell, J. *The PACE Postlaunch Airborne eXperiment (PACE-PAX): Post Campaign Report*; NASA PACE Technical Report Series; Report No. NASA/TM-2025-0011273/Vol. 16; NASA Goddard Space Flight Center: Greenbelt, MD, USA, 2025. [CrossRef]
11. Metrological Traceability: Frequently Asked Questions and NIST Policy. Available online: https://www.nist.gov/metrology/metrological-traceability(accessed on 4 February 2026).
12. Efremova, B. Radiometric Calibration Round Robin for Earth's Reflective Spectral Range. In Proceedings of the Joint Agency Commercial Imagery Evaluation 2026 Workshop, USGS Headquarters, Reston, VA, USA, 13–17 April 2026.
13. Barsi, J.A.; Donley, E.; Goldman, M.; Kampe, T.; Markham, B.L.; McAndrew, B.; McCorkel, J.; Morland, E.; Pedelty, J.A.; Pharr, J.; et al. Prelaunch Spectral Characterization of the Operational Land Imager-2. *Remote Sens.* **2024**, *16*, 981. [CrossRef]
14. Zong, Y.; Brown, S.W.; Johnson, B.C.; Lykke, K.R.; Ohno, Y. Simple spectral stray light correction method for array spectrometers. *Appl. Opt.* **2006**, *45*, 6. [CrossRef] [PubMed]
15. Bouvet, M.; Thome, K.; Berthelot, B.; Bialek, A.; Czapla-Myers, J.; Fox, N.P.; Goryl, P.; Henry, P.; Ma, L.; Marcq, S.; et al. RadCalNet: A radiometric calibration network for Earth observing imagers operating in the visible to shortwave infrared spectral range. *Remote Sens.* **2019**, *11*, 2401. [CrossRef]
16. Guerin, D.C.; Fisher, J.; Graham, E.R. The enhanced MODIS airborne simulator hyperspectral imager. In *Proceedings of the SPIE 8048, Algorithms and Technologies for Multispectral, Hyperspectral, and Ultraspectral Imagery XVII 80480L, Orlando, FL, USA, 25–29 April 2011*; Shen, S.S., Lewis, P.E., Eds.; SPIE: Bellingham, WA, USA, 2011. [CrossRef]
17. Chrisp, M. Convex Diffraction Grating Imaging Spectrometer. U.S. Patent No. 5,880,834, 9 March 1999.
18. Mouroulis, P.; Green, R.O. Review of high fidelity imaging spectrometer design for remote sensing. *Opt. Eng.* **2018**, *57*, 040901. [CrossRef]
19. Fièque, B.; Chorier, P.; Terrier, B. Sofradir detectors for hyperspectral applications from visible up to VLWIR. In *Proceedings of the SPIE 7826, Sensors, Systems, and Next-Generation Satellites XIV 78261I, Toulouse, France, 13 October 2010*; SPIE: Bellingham, WA, USA, 2010. [CrossRef]
20. Brown, S.W.; Eppeldauer, G.P.; Lykke, K.R. NIST facility for spectral irradiance and radiance responsivity calibrations with uniform sources. *Metrologia* **2000**, *37*, 579–582. [CrossRef]
21. McAndrew, B.; Barsi, J.; Sushkov, A.; McCorkel, J. Radiometric Uncertainty Analysis of the GLAMR Calibration Facility. In *Proceedings of the 32nd CALCON Technical Meeting, Logan, UT, USA, 12–15 June 2023*; Utah State University: Logan, UT, USA, 2023. Available online: https://digitalcommons.usu.edu/calcon/calcon2023/All2023Content/5/ (accessed on 7 April 2026).
22. Wang, Z.; Barsi, J.; Thome, K.; Wenny, B.N.; McAndrew, B.; Efremova, B.; McCorkel, J. Uncertainty budget for detector-based absolute radiometric calibration with GLAMR. *Appl. Opt.* **2024**, *63*, 12. [CrossRef] [PubMed]
23. NASA. GLAMR Uncertainty and NIST Radiometer Calibration Reports. Available online: https://glamr.gsfc.nasa.gov/uncertainty (accessed on 4 February 2026).
24. Yoon, H.W.; Gibson, C.E. *NIST Measurement Services: Spectral Irradiance Calibrations*; NIST Special Publication 250-89; NIST: Gaithersburg, MD, USA, 2011. Available online: https://nvlpubs.nist.gov/nistpubs/Legacy/SP/nistspecialpublication250-89.pdf (accessed on 7 April 2026).
25. NASA. EOSDIS Data Processing Levels. Available online: https://www.earthdata.nasa.gov/learn/earth-observation-data-basics/data-processing-levels (accessed on 4 February 2026).
26. NASA. Earthdata Project Page for Western Diversity Time Series. Available online: https://www.earthdata.nasa.gov/data/projects/wdts (accessed on 4 February 2026).
27. Green, R.O.; Eastwood, M.L.; Sarture, C.M.; Chrien, T.G.; Aronsson, M.; Chippendale, B.J.; Faust, J.A.; Pavri, B.E.; Chovit, C.J.; Solis, M.; et al. Imaging spectroscopy and the Airborne Visible/Infrared Imaging Spectrometer (AVIRIS). *Remote Sens. Environ.* **1998**, *65*, 227–248. [CrossRef]
28. NASA. Armstrong Flight Research Center ER-2 Aircraft. Available online: https://airbornescience.nasa.gov/aircraft/ER-2_-_AFRC (accessed on 4 February 2026).
29. Committee on Earth Observation Satellites Working Group on Calibration & Validation. Available online: https://ceos.org/ourwork/workinggroups/wgcv/ (accessed on 4 February 2026).

30. Czapla-Myers, J.; McCorkel, J.; Anderson, N.; Biggar, S. Earth-observing satellite intercomparison using the Radiometric Calibration Test Site at Railroad Valley. *J. Appl. Remote Sens.* **2017**, *12*, 012004. [CrossRef]
31. Czapla-Myers, J.; Thome, K.; Cocilovo, B.; McCorkel, J.; Buchanan, J. Temporal, spectral, spatial study of the automated vicarious calibration test site at Railroad Valley, Nevada. In *Proceedings of the SPIE Earth Observing Systems XIII 7081, San Diego, CA, USA, 10–14 August 2008*; Butler, J.J., Xiong, J., Eds.; SPIE: Bellingham, WA, USA, 2008. [CrossRef]
32. Tonooka, H.; Sakai, M.; Kumeta, A.; Nakau, K. In-Flight Radiometric Calibration of Compact Infrared Camera (CIRC) Instruments Onboard ALOS-2 Satellite and International Space Station. *Remote Sens.* **2020**, *12*, 58. [CrossRef]
33. King, M.D.; Platnick, S.; Wind, G.; Arnold, G.T.; Dominguez, R.T. Remote sensing of radiative and microphysical properties of clouds during TC4: Results from MAS, MASTER, MODIS, and MISR. *J. Geophys. Res.* **2010**, *115*, D00J07. [CrossRef]
34. Meyer, K.; Platnick, S.; Arnold, G.T.; Amarasinghe, N.; Miller, D.; Small-Griswold, J.; Witte, M.; Carins, B.; Gupta, S.; McFarquhar, G.; et al. Evaluating spectral cloud effective radius retrievals from the Enhanced MODIS Airborne Simulator (eMAS) during ORACLES. *Atmos. Meas. Tech.* **2025**, *18*, 981–1011. [CrossRef]
35. McCorkel, J.; Cairns, B.; Wasilewski, A. Imager-to-radiometer in-flight cross calibration: RSP radiometric comparison with airborne and satellite sensors. *Atmos. Meas. Tech.* **2016**, *9*, 955–962. [CrossRef]
36. Smit, J.M.; Rietjens, J.H.H.; van Harten, G.; Di Noia, A.; Laauwen, W.; Rheingans, B.E.; Diner, D.J.; Cairns, B.; Wasilewski, A.; Knobelspiesse, K.D.; et al. SPEX airborne spectropolarimeter calibration and performance. *Appl. Opt.* **2019**, *58*, 5695–5719. [CrossRef] [PubMed]
37. Coddington, O.M.; Richard, E.C.; Harber, D.; Pilewskie, P.; Woods, T.N.; Snow, M.; Chance, K.; Liu, X.; Sun, K. Version 2 of the TSIS-1 Hybrid Solar Reference Spectrum and Extension to the Full Spectrum. *Earth Space Sci.* **2023**, *10*, e2022EA002637. [CrossRef]
38. Palmer, C. *Diffraction Grating Handbook*, 8th ed.; MKS Instruments: Rochester, NY, USA, 2020. Available online: https://api.p1.mks.com/mam/celum/celum_assets/np/resources/MKS_Diffraction_Grating_Handbook.pdf (accessed on 7 April 2026).
39. Thompson, D.R.; Green, R.O.; Bradely, C.; Brodrick, P.G.; Mahowald, N.; Ben Dor, E.; Bennett, M.; Bernas, M.; Carmon, N.; Chadwick, K.D.; et al. On-orbit calibration and performance of the EMIT imaging spectrometer. *Remote Sens. Environ.* **2024**, *303*, 113986. [CrossRef]
40. Angal, A.; McCorkel, J.; Thome, K. Evaluation of GLAMR-based calibration for SI-traceable field reflectance retrievals. In *Proceedings of the Earth Observing Systems XXI, San Diego, CA, USA, 19 September 2016*; Butler, J.J., Xiong, J., Gu, X., Eds.; SPIE: Bellingham, WA, USA, 2016. [CrossRef]
41. Wenny, B.N.; Thome, K.; Czapla-Myers, J. Evaluation of Vicarious Calibration for Airborne Sensors using RadCalNet. *Proc. SPIE* **2020**, *11530*, 1153017. [CrossRef]
42. NASA. Earthdata Search for Data from PACE-PAX. Available online: https://search.earthdata.nasa.gov/search?fpj=PACE-PAX (accessed on 4 February 2026).
43. NASA. Airborne Sensor Facility PACE-PAX Campaign Page. Available online: https://asapdata.arc.nasa.gov/picard/data/deploy_html/pace-pax.html (accessed on 4 February 2026).
44. NASA. Airborne Sensor Facility PICARD WDTS Data. Available online: https://asapdata.arc.nasa.gov/share/PICARD/L1b_Spring2023/ (accessed on 4 February 2026).
45. NASA. Airborne Sensor Facility PICARD PACE-PAX Data. Available online: https://asapdata.arc.nasa.gov/share/PICARD/L1b_PAX2024/(accessed on 4 February 2026).
46. NASA. Armstrong Flight Research Center C-20A (G-III) Aircraft. Available online: https://airbornescience.nasa.gov/aircraft/Gulfstream_C-20A_GIII_-_AFRC (accessed on 4 February 2026).
47. NASA. Johnson Space Center G-III Aircraft. Available online: https://airbornescience.nasa.gov/aircraft/Gulfstream_III_-_JSC (accessed on 4 February 2026).
48. NASA. Langley Research Center G-III Aircraft. Available online: https://airbornescience.nasa.gov/aircraft/Gulfstream_III_-_LaRC (accessed on 4 February 2026).
49. NASA. Johnson Space Center G-V Aircraft. Available online: https://airbornescience.nasa.gov/aircraft/Gulfstream_V_-_JSC (accessed on 4 February 2026).
50. NASA. Armstrong Flight Research Center B200 Aircraft. Available online: https://airbornescience.nasa.gov/aircraft/B200_801_-_AFRC (accessed on 4 February 2026).
51. NASA. Langley Research Center B200 Aircraft. Available online: https://airbornescience.nasa.gov/aircraft/B200_-_LARC (accessed on 4 February 2026).
52. NASA. Earthdata Portal. Available online: https://www.earthdata.nasa.gov (accessed on 4 February 2026).

Disclaimer/Publisher's Note: The statements, opinions and data contained in all publications are solely those of the individual author(s) and contributor(s) and not of MDPI and/or the editor(s). MDPI and/or the editor(s) disclaim responsibility for any injury to people or property resulting from any ideas, methods, instructions or products referred to in the content.